

Bicrystallography-informed Frenkel–Kontorova model for interlayer dislocations in strained 2D heterostructures

Md Tusher Ahmed^a, Chenhaoyue Wang^b, Amartya S. Banerjee^b, Nikhil Chandra Admal^a

^a*Department of Mechanical Science and Engineering University of Illinois at Urbana-Champaign Champaign IL USA*

^b*Department of Materials Science and Engineering University of California Los Angeles. Los Angeles CA USA*

Abstract

In recent years, van der Waals (vdW) heterostructures and homostructures, which consist of stacks of two-dimensional (2D) materials, have risen to prominence due to their association with exotic quantum phenomena originating from correlated electronic states harbored by them. Atomistic scale relaxation effects play an extremely important role in the electronic scale quantum physics of these systems, providing means of manipulation of these materials and allowing them to be tailored for emergent technologies. We investigate such structural relaxation effects in this work using atomistic and mesoscale models, within the context of twisted bilayer graphene — a well-known heterostructure system that features moiré patterns arising from the lattices of the two graphene layers. For small twist angles, atomic relaxation effects in this system are associated with the natural emergence of interface dislocations or strain solitons, which result from the cyclic nature of the generalized stacking fault energy (GSFE), that measures the interface energy based on the relative movement of the two layers. In this work, we first demonstrate using atomistic simulations that atomic reconstruction in bilayer graphene under a large twist also results from interface dislocations, although the Burgers vectors of such dislocations are considerably smaller than those observed in small-twist systems. To reveal the translational invariance of the heterointerface responsible for the formation of such dislocations, we derive the translational symmetry of the GSFE of a 2D heterostructure using the notions of coincident site lattices (CSLs) and displacement shift complete lattices (DSCLs). The workhorse for this exercise is a recently developed Smith normal form bicrystallography framework. Next, we construct a bicrystallography-informed and frame-invariant Frenkel–Kontorova model, which can predict the formation of strain solitons in arbitrary 2D heterostructures, and apply it to study a heterostrained, large-twist bilayer graphene system. Our mesoscale model is found to produce results consistent with atomistic simulations. We anticipate that the model will be invaluable in predicting structural relaxation and for providing insights into various heterostructure systems, especially in cases where the fundamental unit cell is large and therefore, atomistic simulations are computationally expensive.

1. Introduction

Quantum materials, i.e., materials that manifest exotic physical properties due to the presence of strong electronic correlations, have risen to prominence in recent years due to their applications in emergent technologies connected to nanoelectronics and quantum information science [Basov et al., 2017, Keimer and Moore, 2017, Tokura et al., 2017]. The grand challenge of designing and manufacturing such materials stems from the high sensitivity of their properties to local structure and symmetry [Kim et al., 2022]. In recent years, van der Waals (vdW) homostructures and heterostructures, which consist of stacks of two-dimensional (2D) materials, have emerged as an important class of quantum materials [Shimazaki et al., 2020, Jin et al., 2019, Cao et al., 2021, Regan et al., 2020]. The weak vdW interactions between the 2D lattices in such materials offer high fidelity in tuning the local atomic environments, thus allowing exquisite control over the quantum properties of such systems. Small-twist bilayer graphene (BG) is the most prominent example, wherein dispersionless electronic states (or *flat bands*) emerge [Bistritzer and MacDonald, 2011, Tarnopolsky et al., 2019, Cao et al., 2018, Tao et al., 2022, Zhao et al., 2020, 2021] at a specific *magic* twist angle,

Email address: admal@illinois.edu (Nikhil Chandra Admal)

$\theta \sim 1.1^\circ$. Magic-angle twisted BG exhibits unconventional superconductivity, correlated insulator phases, magnetism, and non-trivial topological phases [Papageorgiou et al., 2017, Lee et al., 2019, Cao et al., 2020, Rakib et al., 2022, Uri et al., 2020, Wong et al., 2020] — properties associated with the *moiré superlattice* formed by the constituent 2D lattices. However, such exotic properties are susceptible to perturbations in the twist angle. Since the relative twist between adjoining lattices constitutes only a one-dimensional subspace of the four-dimensional space of relative deformations,¹ we recognize that the larger collection of relative deformation-induced moiré is an exciting test bed to explore new moiré physics. A vdW heterostructure is said to be *heterostrained* if its two lattices are under different strain states [Pochet et al., 2017]. In this paper, we refer to the mutually exclusive twisted and heterostrained states using an umbrella term, *heterodeformation*. The use of heterostrains to tune the electronic properties of materials and explore new quantum states is the goal of *straintronics* [Miao et al., 2021], an emerging research area.

Homostructures such as BGs, under a small twist ($1^\circ - 3^\circ$) relative to the energetically favorable AB stacking, undergo atomic reconstruction due to spontaneous nucleation of interface dislocations, also referred to as *strain solitons*. Recognizing the sensitivity of the electronic properties to atomic rearrangements, strain engineering offers an exciting route to modulate the electronic properties of BGs by controlling the dislocation network using strains [Annevelink et al., 2020, Cazeaux et al., 2023, Cao et al., 2021, Kim et al., 2022]. The overarching goal of this paper — formulated to fully realize the potential of strain engineering for 2D heterostructures — is to *investigate and model atomic reconstruction in heterodeformed moiré superlattices*. Moreover, due to the large size of moiré superlattices, a high-throughput investigation of heterodeformations is computationally challenging, which motivates us to seek a continuum model for atomic reconstruction. In what follows, we will identify the key features of atomic reconstruction observed in small-twist BG before formulating the objectives of this paper.

The atomic reconstruction [Annevelink et al., 2020, Zhang and Tadmor, 2017, 2018, Lopes dos Santos et al., 2012, Carr et al., 2018b, Cazeaux et al., 2020, 2023, Gargiulo and Yazyev, 2017, Zhou et al., 2015] in a small-twist BG is a consequence of the interplay between interfacial energy and the elastic energies of the two lattices. The former is often described using the generalized stacking fault energy (GSFE) density, a periodic function of relative translations between the two AB-stacked lattices of the BG. The periodicity of the GSFE is derived from the bicrystallography of the interacting lattices. Under small twists relative to the AB stacking, the interfacial energy increases as the induced relative translations between the two lattices lead to regions of low-commensurability (high interfacial energy) interspersed with the highly commensurable AB stacking. The twisted BG responds to lower the interfacial energy by an atomic rearrangement that tends to increase (decrease) areas of high (low) commensurability. Due to the periodicity of the GSFE, the structural relaxation results in lines of displacement “jumps” that manifest as interface dislocation lines with the displacement “jump” as the Burgers vector [Alden et al., 2013, Kumar et al., 2016]. Moreover, the Burgers vectors are parallel to the dislocation lines and their magnitude is equal to that of the smallest lattice vector of graphene. Therefore, the structural relaxation in a small-twist BG can be interpreted as elastic distortions associated with the formation of an array of screw lattice dislocations. Since the elastic energy diverges for discontinuous displacements, the “jumps” occur as localized displacement gradients, which implies the dislocation lines are diffused. The balance between the interfacial and elastic energies, which ultimately determines the network and the thickness of the dislocation lines, is at the core of the Frenkel-Kontorova continuum model for small-twist BGs. In this paper, the terms ‘atomic relaxation’ and ‘structural relaxation’ are used synonymously.

Our study of atomic reconstruction in heterodeformed moiré is guided by the energetics of structural relaxation in small-twist BGs. We begin by hypothesizing that the structural relaxation of a heterodeformed moiré is also a consequence of interface dislocations and investigating the hypothesis using atomistic simulations. Instead of a bonafide 2D heterostructure, we use large-twist BG in our atomistic study due to the greater reliability of its interatomic potential, confirmed using Density Functional Theory (DFT). Moreover, it is reasonable to interpret a large-twist BG as a heterostructure since its lattices differ considerably. We show that the 21.786789° large-twist BG, when subjected to heterostrains, results in strain localization in a network of lines, suggesting the formation of interface dislocations. Interestingly, the Burgers vector of the

¹If the two lattices of a heterostructure are subjected to uniform deformation gradients \mathbf{F}_1 and \mathbf{F}_2 , then $\mathbf{F}_1^{-1}\mathbf{F}_2$ is the relative deformation, and its representation as a 2×2 matrix accounts for the four dimensions.

dislocations is smaller than that of the small-twist case.

In the presence of two distinct lattices, the notion of an interface dislocation has to be made precise as it is not clear to which lattice its Burgers vector belongs. The interpretation of a large-twist moiré as a network of lattice screw dislocations breaks down as the dislocation cores overlap. To resolve this ambiguity, we turn our attention to grain/phase boundaries. Similar to a small-twist BG, small-tilt angle grain boundaries can be interpreted as an array of lattice dislocations. For large tilt angles, however, a grain boundary dislocation is defined as a defect in the translation invariance of the boundary [Grimmer et al., 1974]. The translational invariance is derived by introducing two additional lattices — coincident site lattice (CSL) and the displacement shift complete lattice (DSCL) — originating from bicrystallography [Balluffi et al., 1982]. The CSL is the intersection of the two lattices, and the DSCL is the smallest lattice that contains the two lattices. In 2D heterostructures, it is straightforward to see that the CSL *is* the moiré superlattice. On the other hand, the DSCL conveys the translational invariance of the interface — displacing one lattice relative to the other by a DSCL vector preserves the structure of the interface. In other words, if a heterointerface hosts a dislocation, its Burgers vector must be a DSCL vector. While Koda et al. [2016] have used the CSL to identify heterodeformed moirés, the use of DSCL to study interface dislocations remains largely unexplored.² One of the key highlights of this paper is the application of Smith Normal Form (SNF) bicrystallography to characterize interface dislocations. SNF bicrystallography is an algebraic framework developed by the last authors’ group to explore bicrystallography properties such as the translational invariance [Admal et al., 2022]. In particular, it informs us that the Burgers vector (smallest DSCL lattice vector) is inversely proportional and a rational multiple of a CSL vector.

Based on the atomistic simulations of heterodeformed BG and the SNF bicrystallography framework, we build a generalized Frenkel–Kontorova (GFK) model. The generalization relative to the classical Frenkel–Kontorova model stems from key features of the GFK model — frame-invariance and defect-free *natural configurations*, which may include stackings that are not necessarily of the lowest energy.³ The GFK model generalizes the previous model of Nam and Koshino [2017] to large heterodeformations, including large twists. Unlike the model of Nam and Koshino [2017], which was developed exclusively for infinite systems, the model describes finite systems as well, wherein configurational forces due to surface tension play an important role.

This paper is organized as follows. In Section 2, we explore structural relaxation in a BG subjected to large heterodeformations using DFT-informed atomistic simulations and demonstrate the nucleation of interface dislocations. In Section 3, we review SNF bicrystallography and apply it to characterize the interface dislocations in heterodeformed BGs. In Section 4, we build the GFK model and implement and validate it in Section 5. We summarize and conclude in Section 6.

Notation: We use lowercase bold letters to denote vectors, and uppercase bold letters to denote second-order tensors, unless stated otherwise. The gradient, divergence, and curl operators are denoted by the symbols ∇ , Div, and curl respectively. We use the symbol \otimes to denote the tensor product of two vectors, and \cdot to denote the inner product of two vectors or tensors.

2. Atomic scale investigation of structural relaxation under large heterodeformations

This section investigates the structural relaxation of 2D heterostructures using atomistic simulations of heterostrained BG, with the understanding that under large twists, a BG serves as a surrogate for a 2D heterostructure. The relaxation is restricted to being in-plane. Simulations are performed using Large-Scale Atomic/Molecular Massively Parallel Simulator (LAMMPS) [Plimpton, 1995]. Beginning with a small-twist BG, we systematically explore various small and large heterodeformations that result in atomic reconstruction. We will demonstrate that atomic reconstruction due to large heterodeformations results from interface dislocations, whose Burgers vector and the network are markedly different from those observed under small twists. We will revisit the examples of this section in Section 4 using a continuum model.

The simulated BGs are oriented such that the normal to the lattices is along the X_3 direction. Since we allow only in-plane relaxation, the distance between the two graphene lattices is held fixed during the

²A notable exception is the work of Ishikawa et al. [2016] where the DSCL and the moiré superlattice are used to infer the atomic structure of twisted few-layer graphene, which is in the spirit of *moiré metrology* [Annevelink et al., 2021].

³For example, in addition to the AB-stacked BG, a large-twist BG with a twist angle of 21.786789° is also a natural configuration.

	C [meV]	C_0 [meV]	C_2 [meV]	C_4 [meV]	A [meV]	δ [Å]	λ [Å ⁻¹]	z_0 [Å]
KC-1	3.030	15.71	12.29	4.933	10.238	0.578	3.629	3.34.
KC-2	6.678908×10^{-4}	21.847167	12.060173	4.711099	12.660270	0.7718101	3.143921	3.328819.

Table 1: Two parameterizations of the KC potential.

simulation. The intralayer bonding in each graphene sheet is modeled using the reactive empirical bond order (REBO) potential [Brenner et al., 2002]. The interlayer vdW interaction is described using the registry-dependent Kolmogorov–Crespi (KC) potential [Kolmogorov and Crespi, 2005]. We investigate structural relaxation for two parametrizations of the KC potential, denoted as KC-1 [Kolmogorov and Crespi, 2005] and KC-2 [Ouyang et al., 2018] with parameters listed in Table 1. Since the KC-2 model was developed for BG systems under an out-of-plane compression, it may be viewed as an improvement of the KC-1 model. We will, however, explore both KC-1 *and* KC-2 models while investigating large heterodeformations as the qualitative differences in the respective GSFEs lead to markedly different structural relaxations.

Periodic boundary conditions (PBCs) are imposed along two in-plane directions to avoid the influence of free boundary lines. Since PBCs necessitate the existence of a periodic supercell, we are restricted to bilayer configurations wherein the intersection of the projections (on the $X_1 - X_2$ plane) of the two lattices is a 2D superlattice. In other words, PBCs can be enforced if and only a CSL exists. The process of identifying heterodeformations that admit PBCs can be formalized as follows. Two 2D (multi) lattices \mathcal{A} and \mathcal{B} , with structure matrices⁴ \mathbf{A} and \mathbf{B} , respectively, are coincident on a 2D CSL if and only if $\mathbf{T} := \mathbf{A}^{-1}\mathbf{B}$ is a rational matrix. We refer to \mathbf{T} as the *transition* matrix. In a homostructure, if lattice \mathcal{B} is obtained by deforming lattice \mathcal{A} using a deformation gradient \mathbf{F} , then $\mathbf{B} = \mathbf{F}\mathbf{A}$, and all deformations that result in a rational $\mathbf{A}^{-1}\mathbf{F}\mathbf{A}$ yield a CSL, and therefore, amenable to PBCs. In Section 3, we will show that the bicrystallographic properties of a heterodeformed moiré can be deduced from the algebraic properties of the transition matrix. For example, the ratios of the areas of the primitive unit cells —

$$\Sigma_{\mathcal{A}} = \frac{\text{Area}(\text{CSL})}{\text{Area}(\mathcal{A})}, \quad \Sigma_{\mathcal{B}} = \frac{\text{Area}(\text{CSL})}{\text{Area}(\mathcal{B})}, \quad (1)$$

are always integers, and if \mathcal{A} and \mathcal{B} have the same density, $\Sigma_{\mathcal{A}} = \Sigma_{\mathcal{B}} =: \Sigma$. The two basis vectors of the CSL of a heterodeformed moiré are chosen as the in-plane simulation box vectors. Therefore, the number of simulated atoms is equal to $n_{\mathcal{A}}\Sigma_{\mathcal{A}} + n_{\mathcal{B}}\Sigma_{\mathcal{B}}$, where the factors $n_{\mathcal{A}}$ and $n_{\mathcal{B}}$ represents the number of basis atoms in the primitive unit cells of the respective 2D multilattices. In all our simulations, \mathcal{A} is a graphene lattice formed by the structure matrix

$$\mathbf{A} = \frac{a}{2} \begin{bmatrix} 0 & -\sqrt{3} \\ 2 & -1 \end{bmatrix},$$

and \mathcal{B} is a deformation or rotation of \mathcal{A} , and placed at a prescribed interplanar distance in the X_3 direction from \mathcal{A} . The heterodeformed configurations studied in this paper are calculated using an algorithm (see Algorithm 2 in Admal et al. [2022]) derived from Theorem 2 in Appendix A, which generates heterostrained moirés of various sizes and strains within prescribed upper bounds.

Atomic reconstruction is simulated by minimizing the total energy with respect to in-plane displacements of atoms using the fast inertial relaxation engine (FIRE) algorithm [Bitzek et al., 2006] with an energy tolerance and force tolerance of 1×10^{-20} eV and 1×10^{-20} eV Å⁻¹, respectively. The resulting displacements of atoms are analyzed to interpret them in terms of interface dislocations.

2.1. Atomic reconstruction in a BG under a small twist and a small strain

In this section, we present simulations of atomic reconstruction in a BG under two small heterodeformations — a) a 0.2992634° twist and b) a pure stretch of

$$\mathbf{U} = \begin{bmatrix} 1.004219 & 0 \\ 0 & 0.995781 \end{bmatrix} \quad (2)$$

⁴The two basis vectors of a lattice are stored as columns of its structure matrix.

relative to the AB-stacked $\Sigma 1$ configuration. Since the AB-stacked configuration corresponds to $\mathbf{F} = \mathbf{R}(60^\circ)$, lattice \mathcal{B} of the 0.2992634° -twisted BG is constructed using $\mathbf{F} = \mathbf{R}(60.2992634^\circ)$, and for the heterostrained case, $\mathbf{F} = \mathbf{R}(60^\circ)\mathbf{U}$. The interplanar distance is fixed at 3.34 \AA . The basis vectors of the corresponding CSLs,

$$\text{twist: } \mathbf{b}_1 = 470.824979 \mathbf{e}_1, \quad \mathbf{b}_2 = 235.412488 \mathbf{e}_1 + 407.746391 \mathbf{e}_2, \quad \text{and} \quad (3a)$$

$$\text{heterostrain: } \mathbf{b}_1 = -581.794 \mathbf{e}_1, \quad \mathbf{b}_2 = -287.199 \mathbf{e}_1 + 505.965 \mathbf{e}_2, \quad (3b)$$

define the respective periodic boxes of the simulations. From (1) and (3), it follows that $\Sigma = 36\,631$ for the 0.2992634° -twisted BG, whereas $\Sigma_{\mathcal{A}} = 56\,168$ and $\Sigma_{\mathcal{B}} = 56\,169$ for the heterostrained BG.

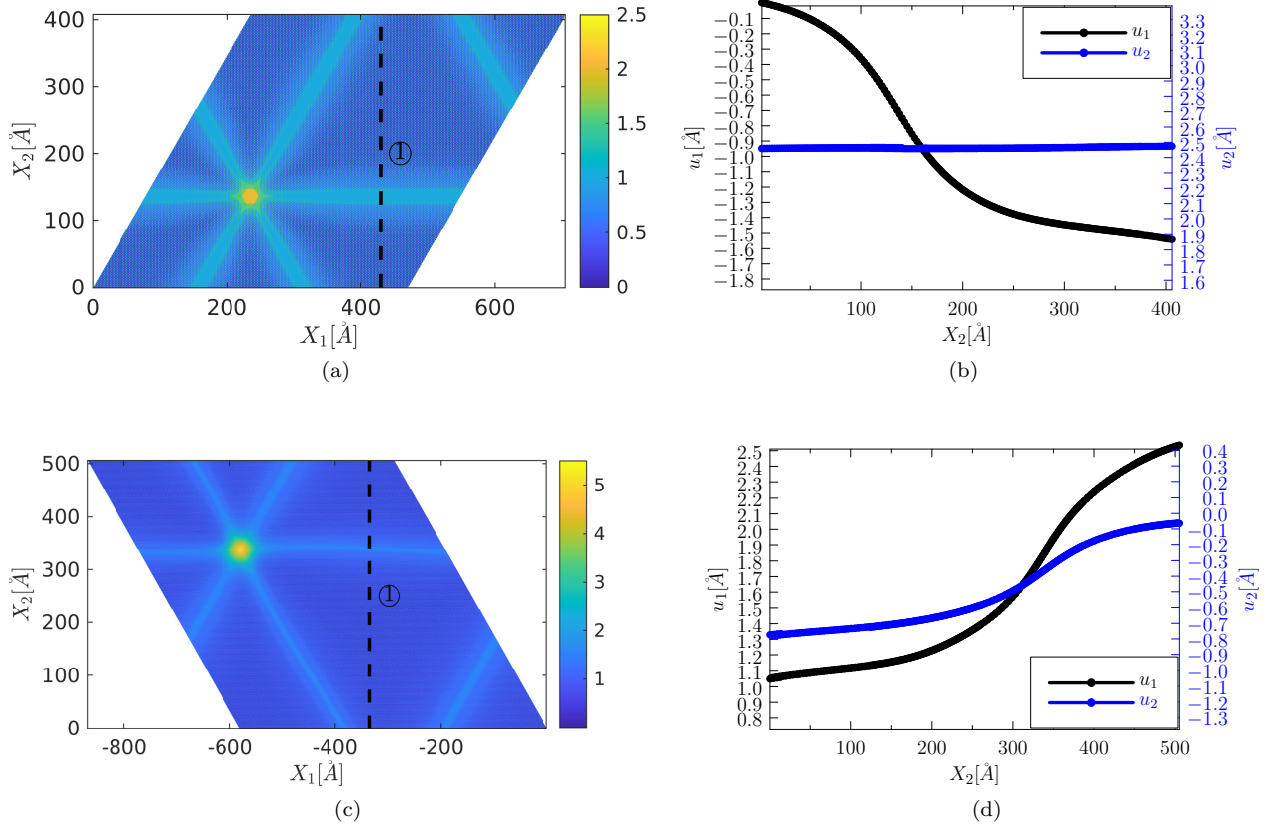


Figure 1: Atomic reconstruction in a BG under a small twist (top row) and a small heterostrain (bottom row). (a), (c) Plots of atomic energy density [meV \AA^{-2}] show a triangular network of interface dislocations. The dislocation lines separate triangular domains of low-energy AB-stacking. (b), (d) Line plots of the displacement components u_1 and u_2 , measured along the dashed lines in (a) and (c). The displacements are measured relative to the untwisted AB-stacked configuration.

The color density plots of atomic energy density shown in Figs. 1a and 1c highlight the triangular dislocation network in the twisted and strained BGs, respectively. The high-energy nodal regions correspond to the AA stacking, and the interiors of the triangular domains are in AB stacking. Figs. 1b and 1d show line plots of displacements of atoms along the dashed lines in the respective energy density plots. The displacements are measured relative to the AB-stacking. Since Fig. 1b shows negligible displacement perpendicular to the dislocation line, interface dislocations in the twisted BG have a screw character. On the other hand, Fig. 1d suggests the interface dislocations in the heterostrained case have a mixed character. In both cases, the Burgers vector magnitude (size of the displacement jump) is $< 2.46 \text{ \AA}$, the lattice constant of graphene, which implies the dislocations are not full dislocations. Annevelink et al. [2020], Pochet et al. [2017] demonstrated that the partial dislocations have a pure edge character under a small biaxial heterostrain relative to the AB stacking.

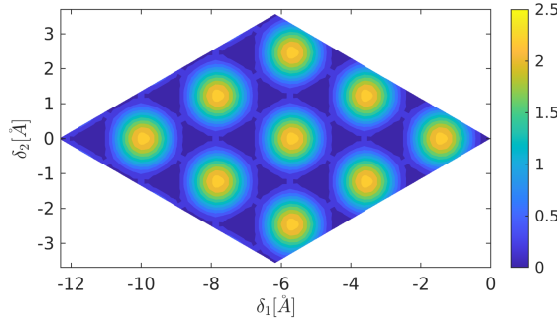


Figure 2: GSFE of AB stacking in $\text{meV } \text{\AA}^{-2}$. The minima and maxima correspond to the AB and AA stackings, respectively. Parametrizations KC-1 and KC-2 yield nearly identical GSFEs.

The origin of interface dislocations and their network pattern can be traced to the properties of AB-stacking’s GSFE, shown in Fig. 2. The GSFE of a BG configuration is a function of the relative displacement between the two layers. The GSFE of AB stacking is periodic with respect to the lattice vectors of graphene. Under small uniform heterodeformations, the relative displacement between the two layers is spatially varying, and therefore, the interfacial energy is sampled from various regions of the GSFE, including the maxima and the minima. The BG responds by an atomic rearrangement to increase (decrease) regions of AB (AA) stacking, which corresponds to minima (maxima) in the GSFE plot, resulting in a juxtaposition of AB-stacked regions separated by dislocation lines. The Burgers vector of a dislocation line separating two AB-stacked regions is the relative vector, with magnitude 1.42 \AA , that connects the corresponding minima in the GSFE.⁵ Moreover, the triangular network of dislocation lines with every AB-stacked region surrounded by three similar regions originates from the observation that each minimum in the GSFE is surrounded by three nearest minima.

The arguments that helped us deduce the properties of dislocations from the GSFE are applicable only under small heterodeformations relative to the AB stacking. Under large heterodeformations, it is not clear if a heterostructure undergoes atomic reconstruction. If reconstruction occurs, its interpretation in terms of full/partial lattice dislocations breaks down as the dislocation cores overlap.⁶

⁵Fig. 1b does not quite recover the entire Burgers vector magnitude of 1.42 \AA as it includes displacements associated with elastic relaxation. In Section 4, where we present our continuum model, we will discuss the procedure to accurately measure the Burgers vector from the displacement field.

⁶As the heterodeformation is measured relative to the AB stacking, the density of interface dislocations increases resulting in dislocation core overlap.

2.2. Atomic reconstruction in a BG under large heterodeformations

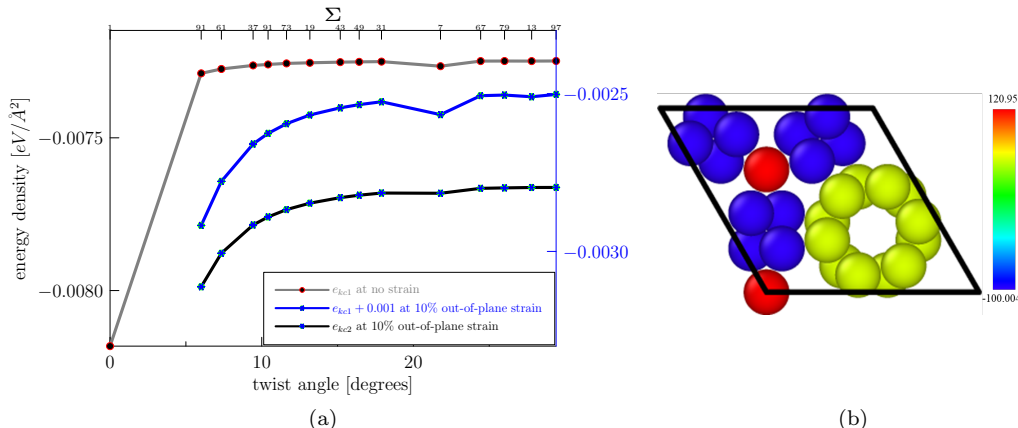


Figure 3: (a) A comparison of interfacial energy density versus the twist angle of a BG under zero strain with that of a BG under a 10% out-of-plane compression. (b) Atomic energy density [meV Å⁻²] within a fundamental unit cell of the $\Sigma 7$ configuration, computed using the KC-1 potential.

It is well known that as the twist angle of a BG increases beyond a few degrees, the vdW interaction between the two lattices weakens, resulting in negligible structural relaxation [Annevelink et al., 2020, Morovati et al., 2022]. Signatures of the presence or absence of interface dislocations can also be found in the plot of interface energy versus the twist angle, shown in Fig. 3a. For small twist angles relative to the AB stacking, the interface energy variation (grey plot) is non-convex — a signature for potential defect nucleation. In contrast, for large twist angles, the interfacial energy is insensitive to the twist angle, and this justifies the absence of atomic reconstruction. While Fig. 3a explores only twists — as opposed to heterodeformations — it is plausible that atomic reconstruction does not occur in heterodeformed configurations far from the AB and AA stackings. However, by decreasing the interlayer distance using external pressure, the interlayer electronic coupling can be made to persist for certain large twist angles. Indeed, this strategy follows the historical trend of using external pressure to probe correlated electron physics. For example, the role of interlayer compression on the atomic reconstruction of 2D heterostructures has been shown to have a substantial influence on the band structure [Carr et al., 2018a, Chittari et al., 2018, Das et al., 2016]. Moreover, experiments and first principle calculations [Hamer et al., 2022, Cheng et al., 2023] have shown that electronic scale effects are modified in large-twist bilayer graphene under out-of-plane compression. The blue plot in Fig. 3a shows that under a 10% out-of-plane strain, the interfacial energy from the KC-1 model is sensitive to twist angles in the neighborhood of 21.786789°. We will refer to the 21.786789°-twist BG as the $\Sigma 7$ configuration. More interestingly, the variation is non-convex in a neighborhood of $\Sigma 7$ twist. Fig. 3b shows the atomic energy densities of the 28 atoms in the unit cell of the $\Sigma 7$ configuration.

The non-convexity of the interfacial energy in the neighborhoods of $\Sigma 1$ and $\Sigma 7$ configurations motivates us to hypothesize that atomic reconstruction occurs for small heterodeformations relative to the $\Sigma 7$ configuration in the presence of an out-of-plane compression. To investigate our hypothesis, we simulate the following two heterodeformations relative to the $\Sigma 7$ configuration — a) a 0.170076° twist and b) a pure stretch of

$$\mathbf{U} = \begin{bmatrix} 1.010589 & 0 \\ 0 & 0.997163 \end{bmatrix}. \quad (4)$$

In other words, the heterodeformations are given by $\mathbf{F} = \mathbf{R}(81.956865^\circ)$ for the former, and $\mathbf{F} = \mathbf{R}(81.786789^\circ)\mathbf{U}$ for the latter case. The box vectors in the two simulations are

$$\text{twist: } \mathbf{b}_1 = 313.233 \mathbf{e}_1, \quad \mathbf{b}_2 = 156.616 \mathbf{e}_1 + 271.267 \mathbf{e}_2, \quad \text{and} \quad (5a)$$

$$\text{heterostrain: } \mathbf{b}_1 = 320.679 \mathbf{e}_1, \quad \mathbf{b}_2 = 1.04735 \mathbf{e}_1 + 548.127 \mathbf{e}_2, \quad (5b)$$

which imply $\Sigma = 16213$, and $\Sigma_{\mathcal{A}} = 33539$ and $\Sigma_{\mathcal{B}} = 33282$, respectively.

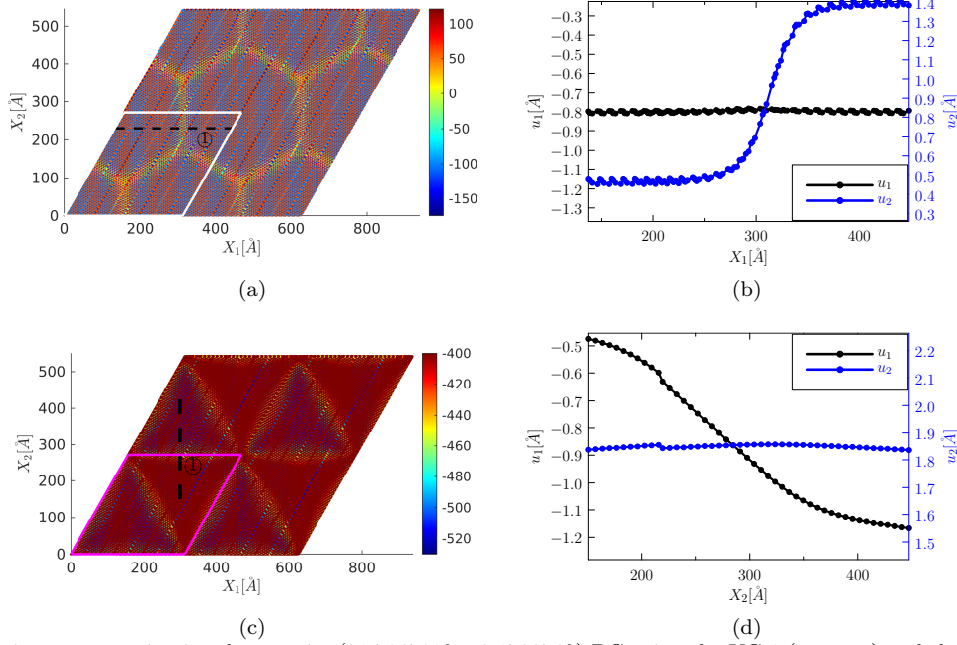


Figure 4: Atomic reconstruction in a large-twist ($21.786789^\circ + 0.170076^\circ$) BG using the KC-1 (top row) and the KC-2 (bottom row) models. (a), (c) Plots of atomic energy density [meV \AA^{-2}] show a honeycomb and a triangular network of interface dislocations. (b), (d) Line plots of the displacement components u_1 and u_2 , measured along the dashed lines in (a) and (c). The displacements are measured relative to the untwisted $\Sigma 7$ configuration.

Fig. 4 shows results of the large-twist simulations using the KC-1 (Figs. 4a and 4b) and KC-2 (Figs. 4c and 4d) models. Comparing the color density plots of atomic energy density in Figs. 4a and 4c, we note that the KC-1 model yields a honeycomb interface dislocation network, while KC-2 results in a triangular network, similar to the small twist case (Fig. 1a). The atomic arrangement in the interiors of the triangular and hexagonal domains is that of the $\Sigma 7$ stacking. The plots in Figs. 4a and 4c are of the atomic energy density relative to the total energy density of the $\Sigma 7$ stacking. Therefore, we expect the energy density in the interior of the triangular/hexagonal domains to be zero. Figs. 4a and 4c, however, do not reflect this due to the variation in the energy densities of the 28 atoms in the primitive unit cell of the $\Sigma 7$.⁷

To identify the nature of the interface dislocations, we plotted (Figs. 4b and 4d) the displacements of atoms along the dashed lines in Figs. 4a and 4c. The displacements are measured relative to the untwisted $\Sigma 7$ stacking. The displacement line plots show negligible displacement perpendicular to the vertical dislocation line, suggesting a screw character. Moreover, the displacement “jumps” suggest the Burgers vector magnitude is \ll than that of the partial dislocations, noted in Section 2.1. Interestingly, the Burgers vector of dislocations from the KC-1 model is larger than those from the KC-2 model. For larger out-of-plane compression, the non-convexity of the interfacial energy increases in the neighborhood of $\Sigma 7$. Therefore, we expect sharper displacement “jumps”, which is confirmed in Fig. 5.

⁷In other words, if the energy densities in Figs. 4a and 4c were spatially averaged using a weighting function with a $\Sigma 7$ unit cell-shaped averaging domain, the resulting fields will be zero in the domain interiors.

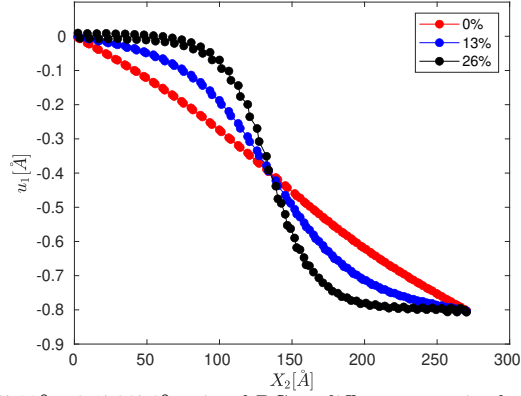


Figure 5: Burgers Vector for $21.786789^\circ + 0.170076^\circ$ twisted BG at different magnitudes of out-of-plane compression calculated using the KC-1 parametrization

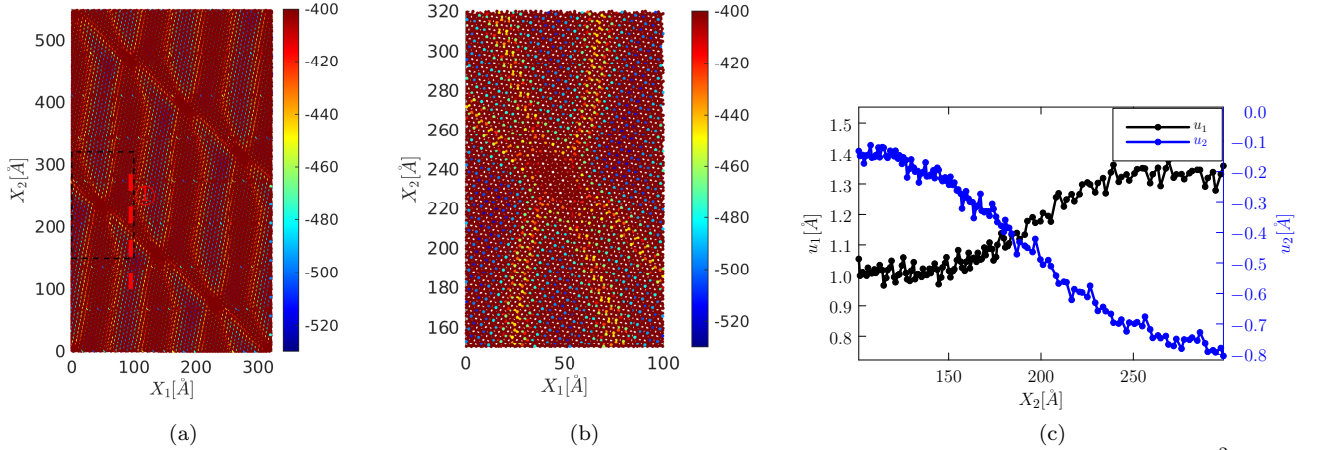


Figure 6: Atomic reconstruction under a large heterodeformation. (a) Color density plot of atomic energy density [$\text{meV } \text{Å}^{-2}$] highlighting the network of interface dislocations in a BG heterodeformed relative to the $\Sigma 7$ configuration using KC-2 parametrization. (b) A magnified view of the dislocation network in (a). (c) shows variations of the displacement components along the dashed line 1, shown in (a). The displacements are measured relative to the $\Sigma 7$ configuration.

Fig. 6 shows simulation results of a BG under large heterodeformation. Similar to the large twist case, we observe interface dislocations that form a distorted triangular network surrounding regions of $\Sigma 7$ stackings. In addition, the displacement line plots along the dashed line in Fig. 6a suggest the dislocations have both screw and edge components, similar to heterostrained BG in Fig. 1c.

Summarizing, this section conclusively demonstrates that atomic reconstruction occurs when a $\Sigma 7$ BG is subjected to small heterodeformations.⁸ Analogous to the AB-stacking, the $\Sigma 7$ configuration is energetically favorable and defect-free. When the $\Sigma 7$ configuration is subjected to a small heterodeformation, atomic reconstruction ensues through strain localization along a network of lines, which we interpret as dislocations. However, we are yet to identify the crystallographic origin of the observed dislocations and their relatively short Burgers vector. In the next section, we will present SNF bicrystallography, an algebraic framework to study the geometric properties of moiré superlattices. In particular, we will apply SNF to arrive at a rigorous definition for interface dislocations that is applicable across all heterodeformations.

⁸Note that while the heterodeformation is small relative to the $\Sigma 7$ configuration, it is large relative to the AB stacking.

3. Bicrystallography and interface dislocations

The goal of this section is to define interface dislocations in 2D heterostructures, including homostructures, under large heterodeformations. An interface dislocation is a line defect that breaks the *translational invariance* of a *defect-free interface*. Low-energy configurations, such as $\Sigma 1$ and $\Sigma 7$ interfaces in a twisted BG, are considered defect-free. In what follows, we will describe a framework to characterize the translational invariance of defect-free interfaces, which ultimately yields the set of interface dislocations a heterointerface can host. Recall from Section 2.1 that the Burgers vector of interface dislocations, formed due to a small heterodeformation of the AB stacking, originates from the GSFE of the AB-stacking. In particular, the periodicity of the GSFE conveys the translational invariance of the interface. This motivates us to investigate the GSFE of the $\Sigma 7$ interface. We use SNF bicrystallography to identify the periodicity of GSFE of a defect-free heterointerface and use it to identify interface dislocations in the $\Sigma 7$ configuration. In what follows, we describe the main results of SNF bicrystallography. For further details, we refer the reader to Algorithm Appendix B and Admal et al. [2022].

SNF bicrystallography is a framework that utilizes the Smith normal form for integer matrices to analyze the bicrystallography of crystal interfaces. It was developed by Admal et al. [2022] to enumerate disconnections (dislocations with a step height) in grain boundaries of simple lattices. Due to the generality of the SNF framework, it is a powerful tool to analyze defects in heterostructures. The open Interface Lab (oILAB), a C++ dimension-independent implementation of SNF bicrystallography archived at <https://github.com/oilab-project/oILAB.git>, was used to generate the heterostructures studied in this paper. The framework begins with two lattices \mathcal{A} and \mathcal{B} — with respective structure matrices \mathbf{A} and \mathbf{B} — that overlap on a lattice $\mathcal{C} := \mathcal{A} \cap \mathcal{B}$, called the *coincident site lattice*. In the context of this paper, \mathcal{A} and \mathcal{B} are 2D multilattices, and \mathcal{C} is a moiré superlattice, which we will assume to be 2D as well. A key step in SNF bicrystallography is the transformation of basis vectors of lattices such that the new basis vectors of the lattices, collected in structure matrices \mathbf{A}^{\parallel} , \mathbf{B}^{\parallel} , and \mathbf{C}^{\parallel} , are parallel. This transformation makes it straightforward to introduce a fourth lattice \mathcal{D} , called the *displacement shift complete lattice* (DSCL), defined as the smallest lattice that contains \mathcal{A} and \mathcal{B} , and therefore \mathcal{C} as well.⁹ Interestingly, the integer algebra of SNF reveals that the ratios of the four lattices are integers, given in terms of integers $\Sigma_{\mathcal{A}}$ and $\Sigma_{\mathcal{B}}$ (defined in (1)), and are related as

$$\det(\mathbf{C}) \det(\mathbf{D}) = \det(\mathbf{A}) \det(\mathbf{B}). \quad (6)$$

Figs. 7a and 7b show the four lattices in the AB-stacked and the $\Sigma 7$ BG configurations, respectively. The two graphene multilattices \mathcal{A} and \mathcal{B} are shown in red and blue. The CSL \mathcal{C} is marked in purple (red+blue), and the DSCL \mathcal{D} in grey. Since $\Sigma = 1$ in the AB-stacked configuration, the four lattices (not including the basis atoms of \mathcal{A} and \mathcal{B}) coincide in Fig. 7a. On the other hand, the DSCL (CSL) in Fig. 7b is 7 times smaller (larger) than the graphene lattice.

The following theorem characterizes the translational invariance of the interface and highlights the importance of the DSCL. The parallel bases vectors resulting from SNF play a critical role in the proof (see Admal et al. [2022]) of the theorem.

Theorem 1. *Translating lattice \mathcal{A} by a vector $\mathbf{b} \in \mathcal{D}$ with \mathcal{B} fixed results in a shift $\lambda_{\mathcal{A}} \in \mathcal{B}$ of the CSL. In other words*

$$(\mathcal{A} + \mathbf{b}) \cap \mathcal{B} = \mathcal{C} + \lambda_{\mathcal{A}}.$$

In addition, the shift is linear in \mathbf{b} , i.e.

$$\lambda_{\mathcal{A}}(\mathbf{b}_1 + \mathbf{b}_2) = \lambda_{\mathcal{A}}(\mathbf{b}_1) + \lambda_{\mathcal{A}}(\mathbf{b}_2), \text{ for any } \mathbf{b}_1, \mathbf{b}_2 \in \mathcal{D}. \quad (7)$$

Fig. 8 conveys the essence of Theorem 1 — translating the shaded region of the red lattice by a DSCL vector (shown in arrows) leads to a CSL shift. However, since the interface structure is preserved, the interfacial energy is identical in the slipped and the non-slipped region, which leads us to the following definition — *an interface dislocation is a line of displacement discontinuity with Burgers vector equal to a DSCL vector*. Moreover, the DSCL translational invariance of the interface implies the GSFE is periodic with respect to the DSCL, and it suffices to describe the GSFE on a primitive unit cell of the DSCL.

⁹ \mathcal{D} is a fictitious lattice as some of its points are unoccupied.

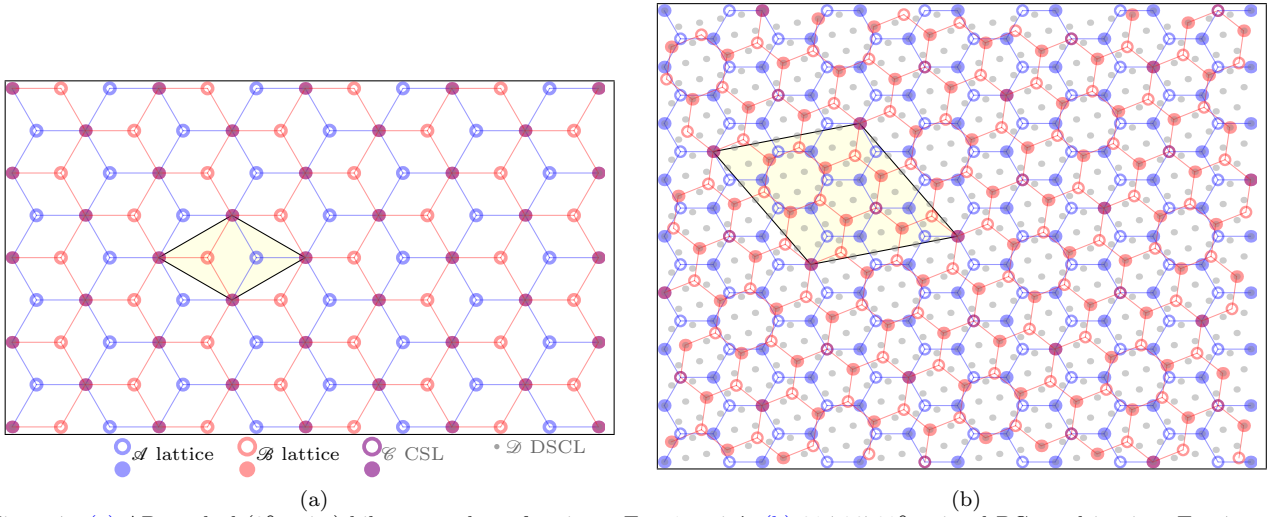


Figure 7: (a) AB-stacked (0° twist) bilayer graphene forming a $\Sigma = 1$ moiré. (b) 21.786789° twisted BG resulting in a $\Sigma = 7$ moiré. Open circles represent the second basis atom of graphene. The two graphene lattices, \mathcal{A} and \mathcal{B} , are shown in blue and red, while the moiré superlattice (\mathcal{E}) and the DSCL (\mathcal{D}) are shown in purple and gray, respectively. The highlighted region represents a unit cell of \mathcal{E} . The ratio of the unit cell size of the moiré superlattice to that of the graphene lattice and the corresponding ratio between the graphene lattice and \mathcal{D} are equal to Σ .

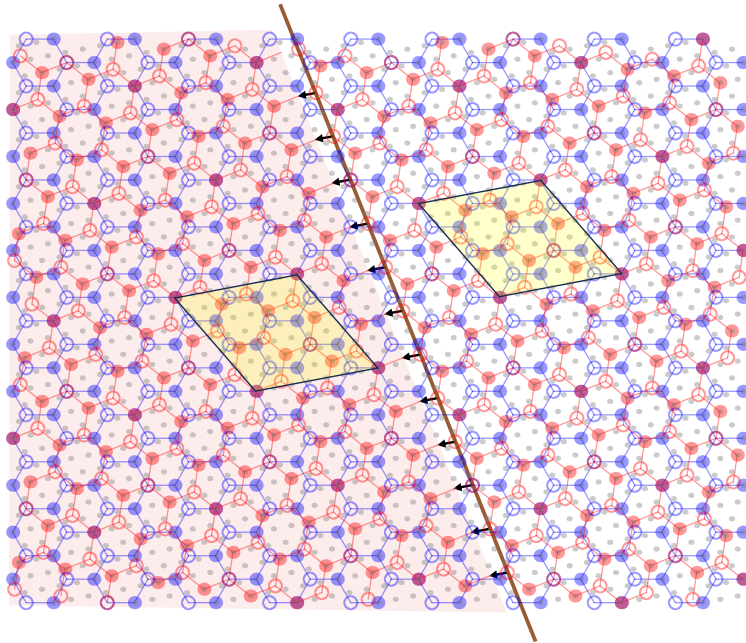


Figure 8: Translational invariance of a 21.786789° twisted BG. Translating the shaded region of the red lattice by a DSCL vector leaves the interface structure invariant and results in a shift in the CSL.

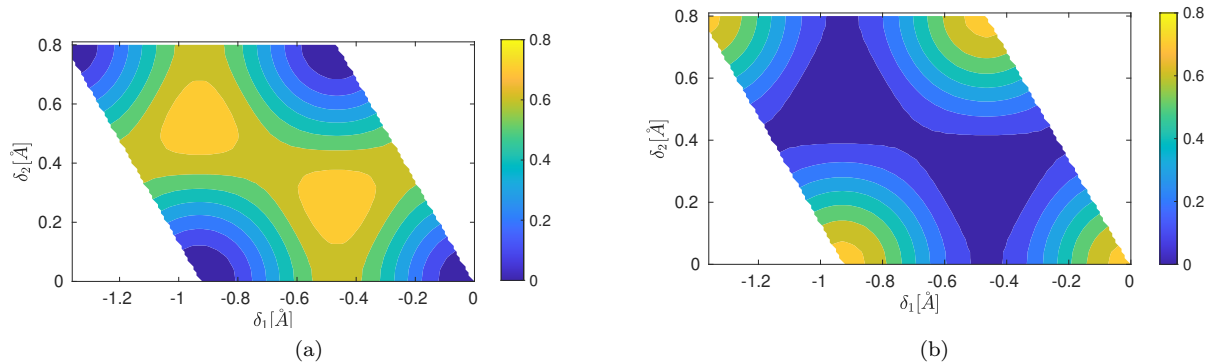


Figure 9: GSFE [$\text{meV } \text{\AA}^{-2}$] plots of $\Sigma 7$ $21.786\ 789^\circ$ twisted BG, computed in LAMMPS using (a) the KC-1 parametrization at a 26% out-of-plane compression, and (b) the KC-2 parametrization at 39% out-of-plane compression.

Using the above definition, we can now revisit Fig. 7 to reason the qualitative differences noted in Section 2 between dislocations in the heterodeformed AB-stacked BG and the $\Sigma 7$ BG configurations. Since the DSCL of an AB-stacked BG is identical to the graphene lattice, its GSFE has the periodicity of graphene, and a dislocation in an AB-stacking is a lattice vector of graphene. However, full dislocations are not observed in an AB-stacking due to degenerate minima in the GSFE, i.e., the GSFE plotted on a primitive unit cell of the DSCL has more than one minimum. Instead, as noted in Section 2.1, partial dislocations form whose Burgers vector is the relative vector connecting two minima of the GSFE. Moving on to the $\Sigma 7$ BG, the magnitude of the smallest non-zero DSCL vector is equal to $2.46/\sqrt{7} = 0.929\ 792\ 153\ \text{\AA}$ (follows from (1) and (6)), which is indeed the displacement jump (see Fig. 4b) observed in the atomistic simulation with the KC-1 parametrization. This implies the line defects in $\Sigma 7$ BG, modeled using KC-1, are full interface dislocations. Fig. 9a shows the GSFE of the KC-1 modeled $\Sigma 7$ BG. The absence of degenerate minima in Fig. 9a justifies the absence of partials in Fig. 4b. However, the GSFE of the KC-2 modeled $\Sigma 7$ BG, shown in Fig. 9b, features two degenerate minima, which suggests the interface dislocations in Fig. 4d are partials. The magnitude of the Burgers vector of the partials can be inferred from Fig. 9b as $2.46/(\sqrt{3}\sqrt{7}) = 0.536\ 816\ \text{\AA}$. In addition to the Burgers vectors, the GSFE also determines the arrangement of the dislocation network. Recall from Section 2.2, that the KC-1 parametrization resulted in a honeycomb dislocation network that separates defect-free $\Sigma 7$ -stacked hexagonal regions. We assert that *the number of sides of the low-energy region is determined by the number of nearest neighbor GSFE minimizers of a minimizer*. This assertion is corroborated by GSFE plots in Fig. 9 — a GSFE minimizer in the KC-2 parameterization has three nearest neighbor minimizers, and therefore, the resulting dislocation network is formed by triangular defect-free $\Sigma 7$ -stackings.

Recall from Section 2.2 that the step character of the displacement “jump” is accentuated as the out-of-plane compression increases. This is because as the two layers are compressed the difference between the maximum and the minimum values of the GSFE, which we will refer to as the *GSFE range width*, increases. We noticed that compared to the KC-1 modeled BG, the KC-2 modeled $\Sigma 7$ BG has a smaller GSFE range width. This was the primary reason we chose a larger out-of-plane compression (39%) in the simulation using the KC-2 model so that the GSFE range widths of the two parametrizations are equal to $0.8\ \text{meV } \text{\AA}^{-2}$, as shown in Fig. 9. Although the GSFE range widths match, the interface dislocations of the KC-2 model are more diffused as the Burgers vector of the partial is smaller by a factor of $\sqrt{3}$. Finally, we verify using density functional theory (DFT) calculations that the KC-2 is superior to KC-1. The DFT-generated GSFE (see Appendix C), plotted in Fig. 10, compares qualitatively well with the GSFE in Fig. 9b. However, from a modeling perspective, the two models are equally valuable as they demonstrate the links between bicrystallography, GSFE, and the properties of interface dislocations.

4. A generalized Frenkel–Kontorova (GFK) model for 2D heterointerfaces

The goal of this section is to build a continuum model to predict structural relaxation in heterostructures subjected to arbitrary heterodeformations by generalizing the Frenkel–Kontorova model of Nam and Koshino

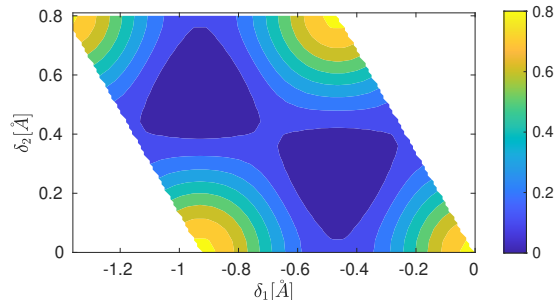


Figure 10: Density functional theory-generated GSFE [$\text{meV } \text{\AA}^{-2}$] of a $\Sigma 7$ 21.786789° twisted BG at a 26% out-of-plane compression.

[2017]. In Section 5, we apply the GFK model to predict structural relaxation in heterodeformed BGs. The kinematics of the GFK model is inspired by the framework of large deformation crystal plasticity [Clayton, 2010, Admal et al., 2018, He and Admal, 2021, Joshi et al., 2022], wherein dislocations are defined with respect to a defect-free natural configuration.

4.1. Kinematics

Consider an interface formed by two 2D (multi) lattices. For simplicity, we will ignore out-of-plane displacement and assume the lattices occupy regions Ω_t^{ref} and Ω_b^{ref} in the 2D Euclidean point space \mathbb{R}^2 .¹⁰ The variable α is used to index the top (t) and bottom (b) layers, i.e., $\alpha = t$ or b . The role of a reference configuration is to measure displacements relative to a fixed configuration, and its choice should not affect the predictions of the model. Since our goal is to isolate and predict displacements associated with atomic reconstruction — as opposed to large-scale deformation — the reference configurations are chosen such that the lattices in $\Omega_\alpha^{\text{ref}}$ are twisted relative to each other or are independently strained uniformly such that they are marginally misaligned relative to a low energy moiré configuration.¹¹ From Section 2, we know that such reference configurations are not stable and undergo atomic reconstruction by nucleating interface dislocations. The goal of this section is to construct *frame-invariant* kinematic measures that quantify the elastic and vdW energies responsible for the atomic reconstruction.

Let $\phi_\alpha : \Omega_\alpha^{\text{ref}} \times [0, \infty] \rightarrow \mathbb{R}^2$ ($\alpha = t, b$) denote time-dependent deformation maps associated with the atomic reconstructions of the respective lattices, measured relative to their reference configurations. The deformed configuration to which ϕ_α maps to will be denoted by Ω_α . Adopting the convention of continuum mechanics, we use \mathbf{X}_α to denote an arbitrary material point in $\Omega_\alpha^{\text{ref}}$. The gradients of the deformation maps are given by $\mathbf{F}_\alpha := \nabla \phi_\alpha$. At this stage, it is useful to connect to the heterostrained moiré example of Section 2, wherein a $\Sigma 7$ moiré twisted BG (21.786789° twist relative to the AB stacking) when subjected to principal stretches of 1.05% and -0.2% , was observed to undergo atomic reconstruction under PBCs. For a continuum analog of this system, the reference configuration will reflect the atomistic system prior to the energy minimization, and $\phi_\alpha - \mathbf{X}_\alpha$ corresponds to the displacements due to energy minimization. If the two lattices in the reference configurations are allowed to relax in the absence of external loads, they will a) return to their respective planar strain-free configurations, and b) twist by an angle that minimizes the vdW energy (as a function of the misorientation angle). In plasticity, this relaxed configuration is commonly referred to as a *natural configuration*.

The idea of a natural configuration plays a central role in our framework as we will show that deformation measures defined with respect to the natural configuration are frame-invariant and independent of the choice of the reference configuration. Employing the language of crystal plasticity theories, we let \mathbf{K}_α represent the map from the tangent space of $\Omega_\alpha^{\text{ref}}$ to that of the natural configuration. In this work, \mathbf{K}_α is a constant tensor, and \mathbf{K}_α^{-1} can be interpreted as the average deformation gradient (relative to the natural configuration) an

¹⁰The out-of-plane displacement during atomic reconstruction is an important feature recently studied by Dai et al. [2016]. While incorporating the out-of-plane displacement into our continuum model is conceptually straightforward, we chose to ignore it to better convey the GFK model.

¹¹This choice is also motivated by the ‘tear and stack’ technique [Kim et al., 2016] to control the twist in a BG.

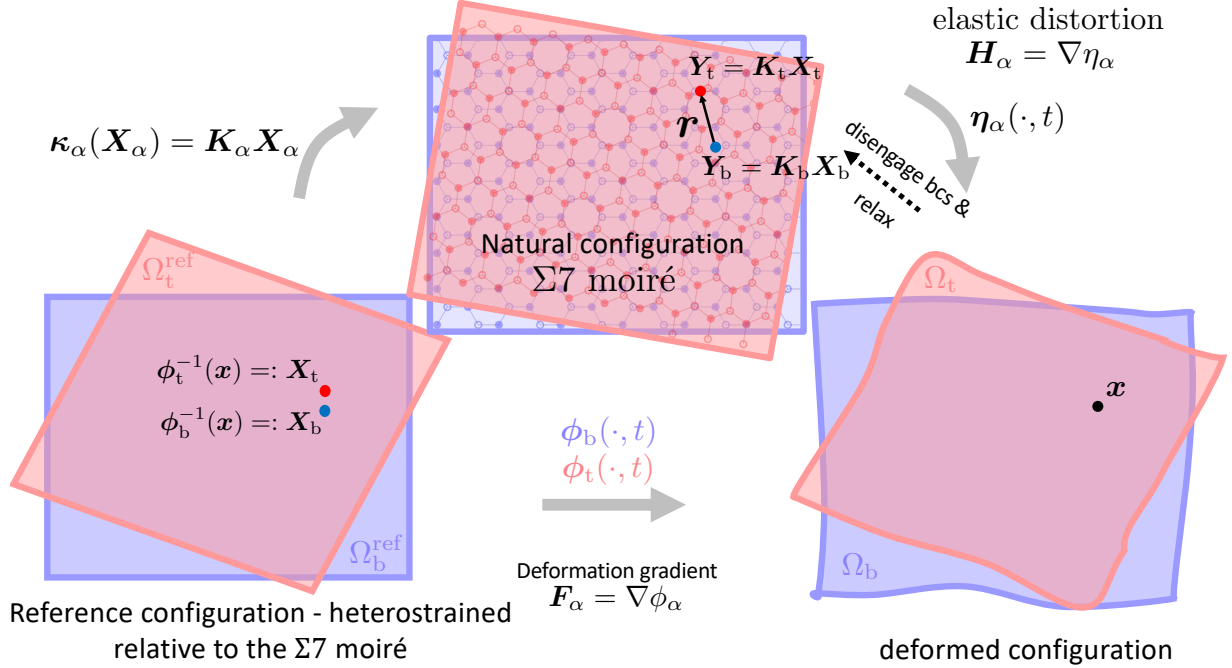


Figure 11: A schematic of the reference (left), natural (middle), and deformed (right) configurations of the GFK model.

experimentalist imposes. The mapping from the reference configuration to the natural configuration is given by $\kappa_\alpha(\mathbf{X}_\alpha) := \mathbf{K}_\alpha \mathbf{X}_\alpha$. Ω_α^n is used to denote a lattice in the natural configuration and points in Ω_α^n will be denoted by \mathbf{Y}_α . Furthermore, we use η_α to denote the mapping from the natural configuration to the deformed configuration. By construction, we have

$$\phi_\alpha = \eta_\alpha \circ \kappa_\alpha, \quad (8)$$

where \circ denotes function composition. From (8), the following relationship between the gradients of the deformation maps follow:

$$\mathbf{F}_\alpha = \mathbf{H}_\alpha \mathbf{K}_\alpha, \text{ where } \mathbf{H}_\alpha := \nabla \eta_\alpha. \quad (9)$$

Note that the gradient in (9) is with respect to \mathbf{Y}_α . Unlike \mathbf{K}_α , \mathbf{H}_α is a time-dependent field, and its inverse describes the relaxation of a local neighborhood of a point $\mathbf{x} \in \Omega_\alpha$ in the absence of external loads. In the context of our heterostrained moiré example, the natural configuration is the $\Sigma 7$ moiré since the two lattices are strain-free and the interfacial energy is minimum in neighborhoods of small hetero-strains and twists. Moreover, $\mathbf{K}_b \equiv \mathbf{I}$ and \mathbf{K}_t^{-1} is equal to the biaxial strain, given in (4).

We will now construct frame-invariant kinematic measures to quantify the elastic and vdW energies. Since the elastic energy due to atomic reconstruction originates from the strains in the lattices measured with respect to a strain-free natural configuration, the relevant frame-invariant kinematic measure is the Cauchy–Green deformation tensor $\mathbf{C}_\alpha := \mathbf{H}_\alpha^T \mathbf{H}_\alpha$. From (9), \mathbf{C}_α can be written as

$$\mathbf{C}_\alpha = \mathbf{K}_\alpha^{-T} \mathbf{F}^T \mathbf{F} \mathbf{K}_\alpha^{-1}. \quad (10)$$

On the other hand, the vdW energy originates from the interaction between lattices in the region $\Omega_t \cap \Omega_b$. The vdW energy is described by the relative translation between the two lattices when allowed to relax to the natural configuration. Therefore, the vdW energy density at a point $\mathbf{x} \in \Omega_t \cap \Omega_b$ will be expressed as a function of the relative vector

$$\mathbf{r}(\mathbf{x}, t) = \mathbf{K}_t \mathbf{X}_t - \mathbf{K}_b \mathbf{X}_b, \text{ where } \mathbf{X}_\alpha := \phi_\alpha^{-1}(\mathbf{x}, t). \quad (11)$$

Summarizing, we have two frame-invariant kinematic measures, \mathbf{C}_α and \mathbf{r} , expressed in terms of the deformation map ϕ_α for given \mathbf{K}_α , that characterize elastic and vdW energies, respectively. In the next section, we will describe the constitutive laws for the elastic and vdW energies in terms of \mathbf{C}_α and \mathbf{r} .

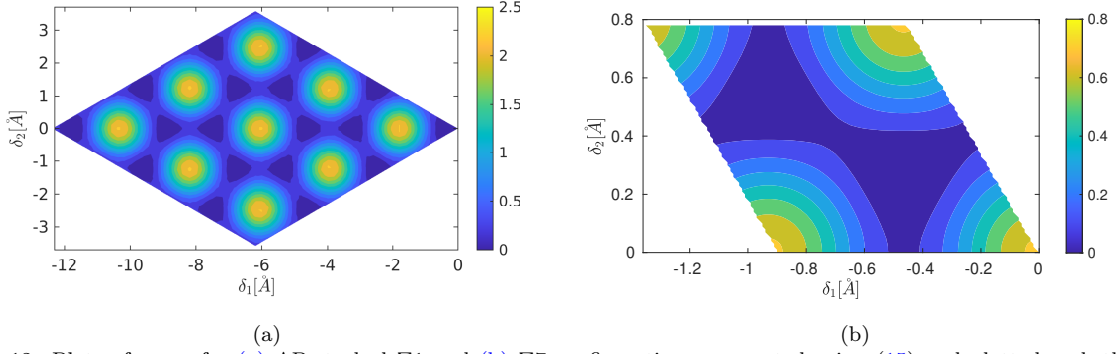


Figure 12: Plots of e_{vdW} for (a) AB-stacked $\Sigma 1$ and (b) $\Sigma 7$ configurations, computed using (15) and plotted such that the minimum is zero.

4.2. Constitutive law

In this section, we construct a frame-invariant energy functional for the GFK model. For prescribed average heterodeformations (\mathbf{K}_α^{-1}), the total energy functional \mathcal{E} is additively decomposed as

$$\mathcal{E}[\phi_t, \phi_b] = \mathcal{E}_{\text{el}} + \mathcal{E}_{\text{vdW}}, \quad (12)$$

into elastic and interfacial energies. Since the elastic energy corresponds to elastic distortions relative to the natural configurations, we assume \mathcal{E}_{el} to be an integral of an elastic energy density (per unit area in the natural configuration) e_{el} over the natural configuration:

$$\mathcal{E}_{\text{el}}[\phi_t, \phi_b] = \sum_{\alpha=t,b} \int_{\Omega_\alpha^n} e_{\text{el}}(\mathbf{E}_\alpha; \alpha) d\mathbf{Y}_\alpha, \quad \text{where } \mathbf{E}_\alpha = (\mathbf{C}_\alpha - \mathbf{I})/2 \quad (13)$$

is the frame-invariant Lagrangian strain tensor, and $e_{\text{el}}(\bullet; \alpha)$ is the elastic energy density of the α -th layer. For example, a Saint Venant–Kirchhoff elastic energy density is of the form $e_{\text{el}} = \mathbb{C}_\alpha \mathbf{E}_\alpha \cdot \mathbf{E}_\alpha / 2$, where \mathbb{C}_α is the fourth-order elasticity tensor of the α -lattice.

The interaction energy term \mathcal{E}_{vdW} measures the changes in the vdW energy due to relative translations between the lattices in the natural configuration. Since the lattices interact in the overlapping region $\Omega_t \cap \Omega_b$ of the deformed configuration, we express \mathcal{E}_{vdW} as an integral over $\Omega_t \cap \Omega_b$ of a vdW energy density e_{vdW} — measured per unit area in the natural configuration. From an atomistic viewpoint, e_{vdW} is the GSF density introduced in Section 2, and is expressed as a function of the frame-invariant relative vector \mathbf{r} introduced in (11). Therefore,

$$\mathcal{E}_{\text{vdW}}[\phi_t, \phi_b] = \frac{1}{2} \sum_{\alpha=t,b} \int_{\Omega_t \cap \Omega_b} (\det \mathbf{H}_\alpha)^{-1} e_{\text{vdW}}(\mathbf{r}(\mathbf{x}_\alpha)) d\mathbf{x}_\alpha. \quad (14)$$

Note that the factor $(\det \mathbf{H}_\alpha)^{-1}$ is necessary because the integration is over the deformed configuration as opposed to the natural configuration. As a result, the interaction energy has to be split evenly between the two lattices leading to the factor of 1/2. From Section 2, we know that e_{vdW} has the periodicity of the DSCL corresponding to the natural configuration. For example, vdW energy densities for the AB stacked- $\Sigma 1$ and the $\Sigma 7$ natural configurations have the form

$$e_{\text{vdW}}(\mathbf{r}) = \pm 2v_0 \sum_{p=1}^3 \cos(2\pi \mathbf{d}^p \cdot (\mathbf{r} + \mathbf{t})) + c, \quad (15)$$

where \mathbf{d}^1 and \mathbf{d}^2 are basis vectors of the reciprocal lattice, $\mathbf{d}^3 = -(\mathbf{d}^1 + \mathbf{d}^2)$, \mathbf{t} is a translation vector, and c and v_0 are constants. By comparing (15) to the atomistics/first principles GSF densities plotted in Figs. 2 and 10 we obtain v_0 and \mathbf{t} corresponding to the $\Sigma 1$ and $\Sigma 7$ configurations. Plots of the resulting e_{vdW} , shown in Fig. 12, compare well with those in Fig. 10.

Next, we propose an evolution law for the unknown fields, ϕ_t and ϕ_b , as a gradient flow of \mathcal{E} :

$$m \dot{\phi}_\alpha = -\delta_{\phi_\alpha} \mathcal{E}, \quad \alpha = t, b \quad (16)$$

where m_α is a prescribed mobility, and δ_{ϕ_α} denotes variation with respect to ϕ_α .

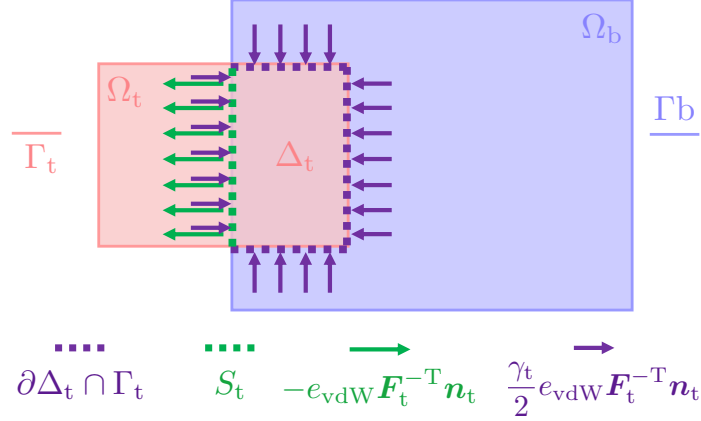


Figure 13: A schematic showing two types of tractions (purple and green arrows) on the boundary of the overlapping region, $\Delta_t \subset \Omega_t$, due to surface tension associated with vdW interactions in a finite 2D heterostructure. The traction forces balance the thermodynamic driving forces that act to increase the region of overlap. The purple arrows are compressive forces associated with the overlapping region's tendency to dilate to increase its area. The green arrows are configurational forces on S_t that balance the thermodynamic forces conjugate to aerial changes in Δ_t due to the translation of Ω_t into Ω_b .

4.3. Derivation of the governing equations of the GFK model

In this section, we derive the governing equations of the GFK model by calculating the variational derivative in (16). The derivation is applicable to finite systems, a notable departure from earlier works, which focused on infinite systems modeled using PBCs. In addition to the critical role vdW energy plays in the structural relaxation of 2D heterostructures, we will show that it manifests as surface tension, which contributes towards configurational forces on the two lattices.

To compute the variation with respect to ϕ_α , we transform the integrals in (13) and (14) to the reference configurations. We begin by rewriting the elastic energy in (13) by noting that $d\mathbf{Y}_\alpha = (\det \mathbf{K}_\alpha) d\mathbf{X}_\alpha$:

$$\mathcal{E}_{\text{el}}[\phi_t, \phi_b] = \sum_{\alpha=t,b} \int_{\Omega_\alpha^{\text{ref}}} e_{\text{el}}(\mathbf{E}_\alpha; \alpha) J_\alpha d\mathbf{X}_\alpha, \quad (17)$$

where $J_\alpha := \det \mathbf{K}_\alpha$. Taking the variation of \mathcal{E}_{el} in (17) with respect to ϕ_α , we obtain

$$-\delta_{\phi_\alpha} \mathcal{E}_{\text{el}} = J_\alpha \text{Div}(\mathbf{P}_\alpha) \text{ in } \Omega_\alpha^{\text{ref}}, \text{ where } \mathbf{P}_\alpha := \mathbf{H}_\alpha \nabla e_{\text{el}} \mathbf{K}_\alpha^{-T}. \quad (18)$$

The tensor \mathbf{P}_α is the 2D analog of the elastic Piola–Kirchhoff stress, which measures force in Ω_α measured per unit length in $\Omega_\alpha^{\text{ref}}$. In addition, the variational derivative also yields the usual expression for the traction on the boundary Γ_α of Ω_α as $\mathbf{P}_\alpha \mathbf{n}_\alpha$, where \mathbf{n}_α is a outward unit vector normal to $\Gamma_\alpha^{\text{ref}}$.

Compared to (18), calculating the variation of \mathcal{E}_{vdW} in (14) is a delicate exercise due to a) the presence of the inverse function ϕ_α^{-1} , and b) the domain of integration in (14) is a part of the deformed configuration and is therefore sensitive to ϕ_α . We begin with $\delta_{\phi_t} \mathcal{E}_{\text{vdW}}$. To eliminate the dependence on ϕ_t^{-1} , we transform the two domains of integration in (14) to $\Delta_t^{\text{ref}} := \phi_t^{-1}(\Omega_t \cap \Omega_b)$ in the reference configuration by noting that $d\mathbf{x}_t = d\mathbf{x}_b = (\det \mathbf{F}_t) d\mathbf{X}_t$, resulting in

$$\mathcal{E}_{\text{vdW}}[\phi_t, \phi_b] = \frac{J_t}{2} \int_{\Delta_t^{\text{ref}}} \left(1 + \underbrace{\det(\mathbf{H}_t \mathbf{H}_b^{-1})}_{\gamma_t} \right) e_{\text{vdW}}(\mathbf{r}_t(\mathbf{X}_t)) d\mathbf{X}_t. \quad (19)$$

where $\mathbf{r}_\alpha(\mathbf{X}_\alpha) := \mathbf{r}(\mathbf{x})|_{\mathbf{x}=\phi_\alpha(\mathbf{X}_\alpha)}$, i.e.

$$\mathbf{r}_t(\mathbf{X}_t) = \mathbf{K}_t \mathbf{X}_t - \mathbf{K}_b(\phi_b^{-1} \circ \phi_t(\mathbf{X}_t)) \text{ and } \mathbf{r}_b(\mathbf{X}_b) = \mathbf{K}_t(\phi_t^{-1} \circ \phi_b(\mathbf{X}_b)) - \mathbf{K}_b \mathbf{X}_b. \quad (20)$$

From (20), we note that the integrand in (19) depends on ϕ_t and its gradient but not its inverse, as desired. The variational derivative of (19) with respect to ϕ_t now follows:

$$-\delta_{\phi_t} \mathcal{E}_{\text{vdW}} = J_t \left[\frac{1 + \gamma_t}{2} \mathbf{H}_b^{-T} \nabla e_{\text{vdW}} + \text{Div} \left(\frac{\gamma_t}{2} e_{\text{vdW}} \mathbf{F}_t^{-T} \right) \right] \text{ in } \Delta_t^{\text{ref}}. \quad (21)$$

along with two kinds of traction forces

$$\frac{\gamma_t}{2} e_{\text{vdW}} \mathbf{F}_t^{-\text{T}} \mathbf{n}_t \text{ on } \partial\Delta_t^{\text{ref}}, \quad (22a)$$

$$-\frac{1+\gamma_t}{2} e_{\text{vdW}} \mathbf{F}_t^{-\text{T}} \mathbf{n}_t \text{ on } S_t := \partial\Delta_t^{\text{ref}} - \Gamma_t^{\text{ref}}. \quad (22b)$$

The expression ∇e_{vdW} in (21) seeks to increase areas of high commensurability, and is responsible for the formation of interface dislocations. The term $e_{\text{vdW}}\gamma_t/2$ in (21) is the surface tension/pressure that is conjugate to aerial changes in Ω_t , and (22a) is the corresponding traction. The traction in (22a) acts to counter the thermodynamic driving force that tends to dilate Ω_t — since e_{vdW} is negative — to maximize the area of overlap with Ω_b . Therefore, the traction in (22a) is compressive, as the purple arrows in Fig. 13 depict. On the other hand, the traction in (22b), shown in green in Fig. 13, is a configurational force that acts on the part of $\partial\Delta_t^{\text{ref}}$ that belongs to the interior of Ω_t . It works to oppose the thermodynamic driving force that translates Ω_t into Ω_b , thereby increasing the area of overlap.¹² Notice that the boundary S_t experiences both tractions mentioned in (22), as shown in Fig. 13. Therefore, the total traction on $\partial\Delta_t$ due to vdW interactions is given by

$$-e_{\text{vdW}} \mathbf{F}_t^{-\text{T}} \mathbf{n}_t \text{ on } S_t, \text{ and} \quad (23a)$$

$$\frac{\gamma_t}{2} e_{\text{vdW}} \mathbf{F}_t^{-\text{T}} \mathbf{n}_t \text{ on } \partial\Delta_t^{\text{ref}} - S_t. \quad (23b)$$

Substituting (18) and (21) into (16), results in a governing equation for Ω_t :

$$m_t \dot{\phi}_t = \begin{cases} \text{Div}(\mathbf{P}_t + \frac{\gamma_t}{2} e_{\text{vdW}} \mathbf{F}_t^{-\text{T}}) + \frac{1+\gamma_t}{2} \mathbf{H}_b^{-\text{T}} \nabla e_{\text{vdW}}(\mathbf{r}_t) \text{ in } \Delta_t, \\ \text{Div}(\mathbf{P}_t) \text{ in } \Omega_t - \Delta_t, \end{cases} \quad (24)$$

where $m_\alpha := J_\alpha^{-1} m$, along with traction boundary conditions in (23). Similarly, the governing equation for Ω_b is given by

$$m_b \dot{\phi}_b = \begin{cases} \text{Div}(\mathbf{P}_b + \frac{\gamma_b}{2} e_{\text{vdW}} \mathbf{F}_b^{-\text{T}}) - \frac{1+\gamma_b}{2} \mathbf{H}_t^{-\text{T}} \nabla e_{\text{vdW}}(\mathbf{r}_b) \text{ in } \Delta_b, \\ \text{Div}(\mathbf{P}_b) \text{ in } \Omega_b - \Delta_b, \end{cases} \quad (25)$$

where $\gamma_b := \det(\mathbf{H}_b \mathbf{H}_t^{-1})$, along with corresponding traction boundary conditions. A notable feature of the governing equations is that the total stress now includes a contribution from surface tension, which was absent in previous Frenkel–Kontorova models that were developed for infinite systems. While the role of surface tension may be ignored for infinite systems, we expect it to play an important role in finite systems, wherein sliding between the constituent 2D lattices is enhanced. It is worth pointing out that the two key features of our model — surface tension and frame-invariance¹³ — are a consequence of the model’s geometrically nonlinear kinematic framework.

Next, we will focus our attention on using the GFK model to simulate atomic reconstruction in infinite 2D heterostructures and compare its predictions with atomistic simulation results of Section 2. To this end, we simplify our model for numerical implementation by ignoring the surface tension terms and assuming $J_\alpha \approx 1$, resulting in

$$m \dot{\phi}_t = \text{Div}(\mathbf{P}_t) + \mathbf{H}_b^{-\text{T}} \nabla e_{\text{vdW}}(\mathbf{r}_t), \quad (27a)$$

$$m \dot{\phi}_b = \text{Div}(\mathbf{P}_b) - \mathbf{H}_t^{-\text{T}} \nabla e_{\text{vdW}}(\mathbf{r}_b). \quad (27b)$$

¹²Mathematically, the configurational force on S_t arises due to the dependence of Δ_t^{ref} (the domain of integration in (19)) on ϕ_t .

¹³Indeed, under an arbitrary superposed rigid body displacement given by a constant rotation tensor \mathbf{R} and a constant vector \mathbf{c} , the fields transform to

$$\tilde{\phi}_\alpha = \mathbf{R} \phi_\alpha + \mathbf{c}; \quad \tilde{\mathbf{F}}_\alpha = \mathbf{R} \mathbf{F}_\alpha (\implies \tilde{\mathbf{H}}_\alpha = \mathbf{R} \mathbf{H}_\alpha); \quad \tilde{\boldsymbol{\sigma}}_\alpha = \boldsymbol{\sigma}_\alpha; \quad \tilde{\mathbf{K}}_\alpha = \mathbf{K}_\alpha; \quad \tilde{\mathbf{r}}_\alpha = \mathbf{r}_\alpha, \quad (26)$$

and continue to satisfy (27).

Using (20) and recalling from (9) that $\mathbf{H}_\alpha = \mathbf{F}_\alpha \mathbf{K}_\alpha^{-1}$, the right-hand-side of (27) can be expressed entirely in terms of the unknown ϕ_α , its gradient, and its inverse. However, the dependence on the inverse is impractical for numerical computation. Therefore, we resort to approximating¹⁴ \mathbf{r}_t and \mathbf{r}_b as

$$\mathbf{r}_t \approx (\mathbf{K}_t - \mathbf{K}_b) \mathbf{X}_t - \mathbf{H}_b^{-1}(\phi_t(\mathbf{X}_t) - \phi_b(\mathbf{X}_t)), \quad (30a)$$

$$\mathbf{r}_b \approx (\mathbf{K}_t - \mathbf{K}_b) \mathbf{X}_b - \mathbf{H}_t^{-1}(\phi_t(\mathbf{X}_b) - \phi_b(\mathbf{X}_b)). \quad (30b)$$

The above approximation preserves the frame-invariance of the model. In the next section, we will present a numerical implementation of (27) with the \mathbf{r}_α -approximation in (30).

5. Numerical implementation of the GFK model and comparison with atomistics

The goal of this section is to implement the GFK model by solving (27) numerically under PBCs, simulate atomic reconstruction in heterostrained small- and large-twist BGs, and validate the continuum model by comparing to atomistics. While the GFK model applies to finite and infinite domains, we restrict the numerical implementation to periodic systems as the primary goal is to compare to the periodic atomistic simulations of Section 2.

Inputs to the model include —

- the top lattice \mathcal{A} and the bottom lattice \mathcal{B} of the natural configuration, which form a moiré supercell. For example, the AB-stacking and the $\Sigma 7$ configurations;
- the average heterodeformations \mathbf{K}_α^{-1} imposed on the natural configuration, which determine the reference configuration. We take $\mathbf{K}_b = \mathbf{I}$, and \mathbf{K}_t^{-1} is chosen from the set of heterodeformations that ensure the reference configuration satisfies PBCs, i.e. lattices \mathcal{A} and $\mathbf{K}_b^{-1}\mathcal{B}$ share a CSL. A primitive unit cell of this CSL is chosen as the reference configuration and the simulation domain. For example, when AB-stacking is the natural configuration, \mathbf{K}_b^{-1} is a 0.2992634° twist or the heterostrain in (2). When $\Sigma 7$ is the natural configuration, \mathbf{K}_b^{-1} is a 0.170076° twist or the strain in (4).
- isotropic elastic constants of graphene: $\lambda = 3.5 \text{ eV } \text{\AA}^{-2}$ and $\mu = 7.8 \text{ eV } \text{\AA}^{-2}$; and
- the constant v_0 of the vdW energy density in (15). For the AB-stacking, v_0 is equal to $0.25 \text{ meV } \text{\AA}^{-2}$, and for the $\Sigma 7$ configuration, it is set to $-0.08 \text{ meV } \text{\AA}^{-2}$ and $0.08 \text{ meV } \text{\AA}^{-2}$ corresponding to the KC-1 and KC-2 potentials, respectively.
- the mobilities m_α , which are chosen as unity.

5.1. Numerical method

PBCs offer the advantage of the fast Fourier transform (FFT) to compute spatial gradients, and therefore, we use the pseudospectral method [Hussaini and Zang, 1987] to solve the governing equation in (27). Spatial

¹⁴ \mathbf{r}_t and \mathbf{r}_b can be expressed as

$$\mathbf{r}_t = \mathbf{K}_t \mathbf{X}_t - \mathbf{K}_b \mathbf{X}_b = (\mathbf{K}_t - \mathbf{K}_b) \mathbf{X}_t + \mathbf{K}_b (\mathbf{X}_t - \mathbf{X}_b), \quad (28a)$$

$$\mathbf{r}_b = \mathbf{K}_t \mathbf{X}_t - \mathbf{K}_b \mathbf{X}_b = \mathbf{K}_t (\mathbf{X}_t - \mathbf{X}_b) + (\mathbf{K}_t - \mathbf{K}_b) \mathbf{X}_b. \quad (28b)$$

Since $\phi_t(\mathbf{X}_t) = \phi_b(\mathbf{X}_b)$, it follows that

$$\phi_t(\mathbf{X}_t) - \phi_b(\mathbf{X}_t) = \phi_b(\mathbf{X}_b) - \phi_b(\mathbf{X}_t) \approx \mathbf{F}_b(\mathbf{X}_b - \mathbf{X}_t),$$

$$\phi_t(\mathbf{X}_b) - \phi_b(\mathbf{X}_b) = \phi_t(\mathbf{X}_b) - \phi_t(\mathbf{X}_t) \approx \mathbf{F}_t(\mathbf{X}_b - \mathbf{X}_t),$$

which imply

$$\mathbf{X}_t - \mathbf{X}_b \approx -\mathbf{F}_b^{-1}(\phi_t(\mathbf{X}_t) - \phi_b(\mathbf{X}_t)), \quad (29a)$$

$$\mathbf{X}_t - \mathbf{X}_b \approx -\mathbf{F}_t^{-1}(\phi_t(\mathbf{X}_b) - \phi_b(\mathbf{X}_b)). \quad (29b)$$

Equation (28a) and the approximation (29a) yield (30a). Similarly, (28b) and (29b) result in (30b).

gradients in (27) are computed using FFT and the solution is marched forward in time using the Runge–Kutta (RK) explicit time integration with a fixed time step δt , resulting in the following discretized equations:

$$\phi_\alpha^{n+1} = \phi_\alpha^n + \frac{1}{6m} (\mathbf{k}_{\alpha 1} + 2\mathbf{k}_{\alpha 2} + 2\mathbf{k}_{\alpha 3} + \mathbf{k}_{\alpha 4}), \text{ where}$$

$$\mathbf{k}_{\alpha 1} = \delta t \mathbf{f}_\alpha|_{\phi=\phi^n}, \quad \mathbf{k}_{\alpha 2} = \delta t \mathbf{f}_\alpha|_{\phi=\phi^n + \frac{\mathbf{k}_{\alpha 1}}{2}}, \quad \mathbf{k}_{\alpha 3} = \delta t \mathbf{f}_\alpha|_{\phi=\phi^n + \frac{\mathbf{k}_{\alpha 2}}{2}}, \quad \mathbf{k}_{\alpha 4} = \delta t \mathbf{f}_\alpha|_{\phi=\phi^n + \mathbf{k}_{\alpha 3}}.$$

Here, $\phi_\alpha^n := \phi_\alpha(\cdot, t_n)$, \mathbf{f}_α represents the right-hand-side of (27), and $\mathbf{f}_\alpha|_{\phi=\phi^n}$ denotes the evaluation of \mathbf{f}_α using ϕ_α^n . The spatial derivatives in \mathbf{f}_α are computed using FFT. The simulation domain was discretized using a 128×128 grid, and $\delta t = 0.1$ sec was the time step size. The spatial discretization was chosen such that the width of the interface dislocations is reasonably resolved, and the temporal discretization is fixed to ensure the numerical scheme remains stable.

All simulations are run long enough to ensure the elastic and the vdW energies converge. Since $\phi_\alpha^0 \equiv \mathbf{0}$, the elastic energy at $t = 0$ is zero and the vdW energy is the only contributor to the total energy. As the simulation progresses, elastic energy increases and the vdW energy decreases, such that the total energy monotonically decreases.

5.2. Comparison with atomistics

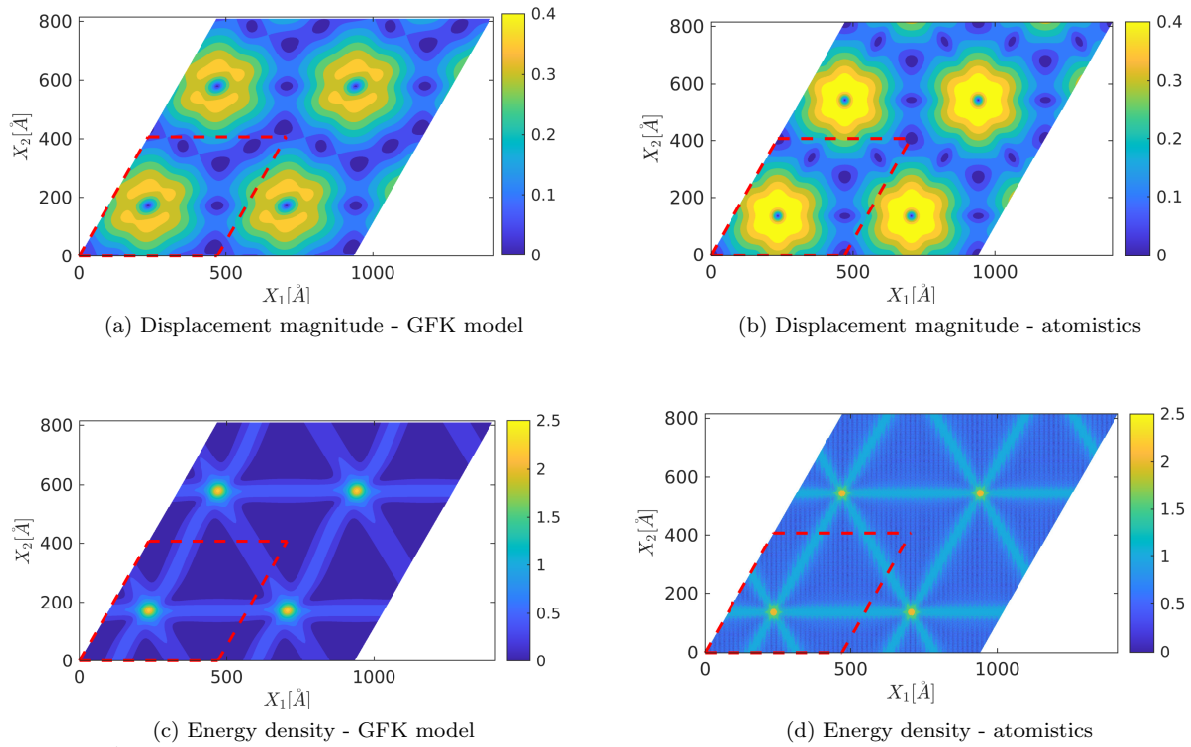


Figure 14: A comparison of structural relaxation predicted by continuum and atomistics simulations of a 0.2992634° small-twist BG. The units of energy density and displacement are $\text{meV } \text{\AA}^{-2}$ and \AA , respectively. The area enclosed by the red dashed line is the simulation domain.

We will now present continuum simulations and compare them to atomistic simulations of heterodeformed BGs, discussed in Section 2. The first column of Fig. 14 shows plots of the displacement magnitude and the total energy density in a 0.2992634° small-twist BG. They compare well with the corresponding plots from the atomistic simulation, shown in the second column. The area enclosed by the red dashed line is the simulation domain. The plots are presented on an extended domain to highlight the triangular network of dislocations.

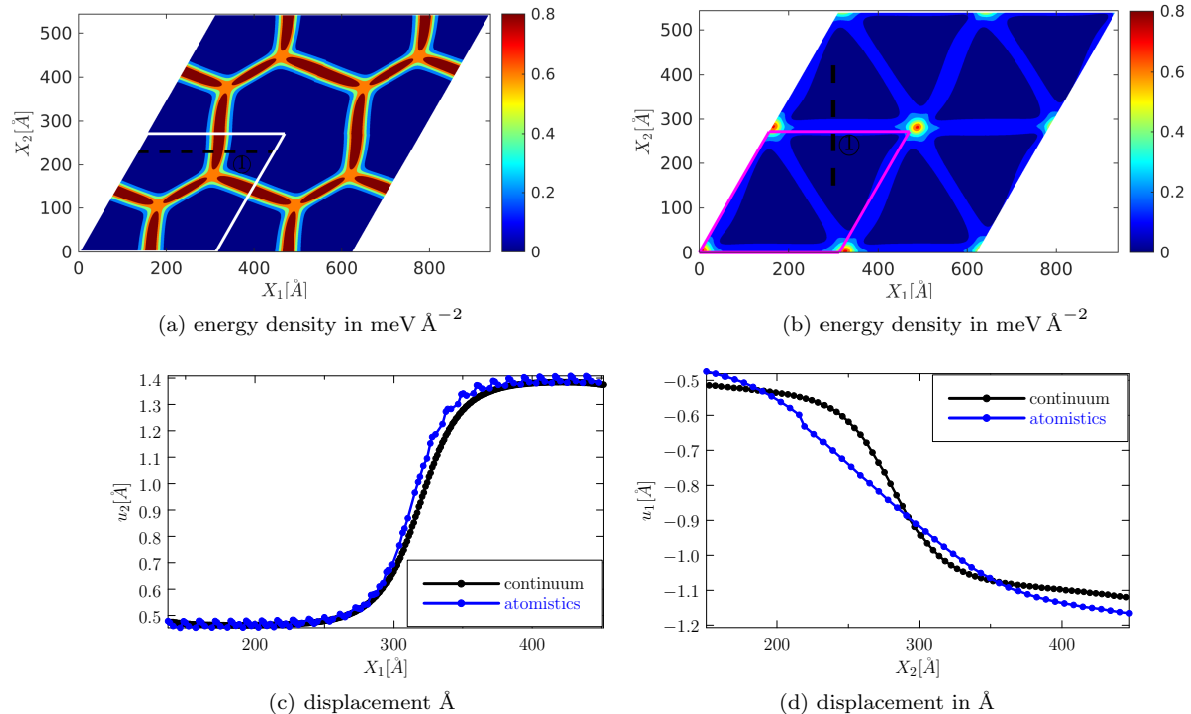


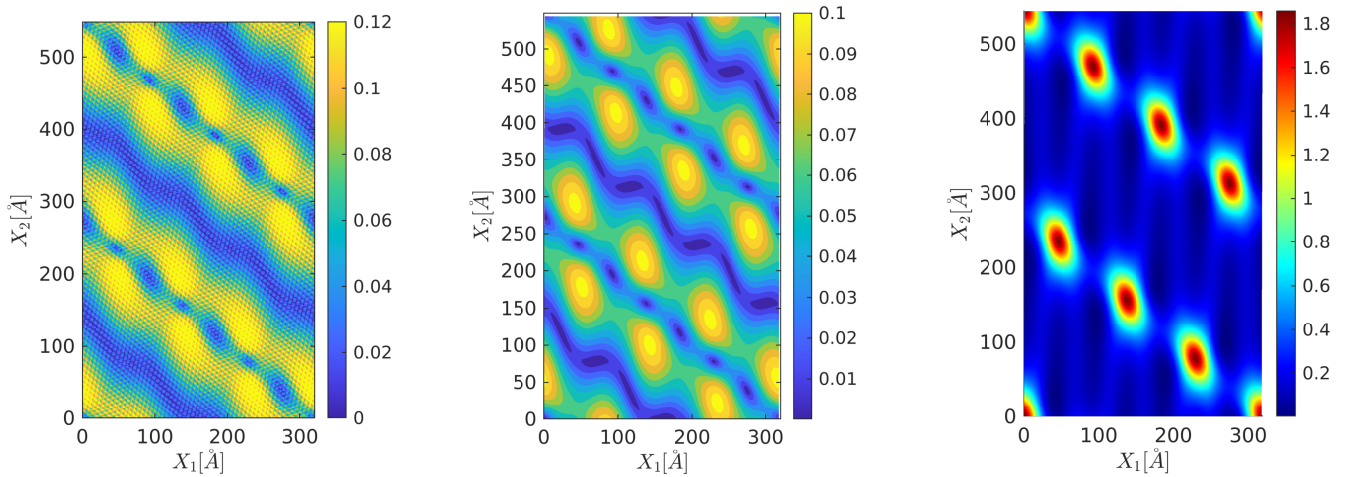
Figure 15: Structural relaxation in a 21.956865 Å large-twist BG using the KC-1 and KC-2 parametrizations. The energy density plots in (a) and (b) highlight the honeycomb and the triangular network of interface dislocations, corresponding to KC-1 and KC-2 models, respectively. (c) and (d) compare the displacement across the dashed lines predicted by the atomistic and the FK models.

Fig. 15 shows continuum simulation results of a 21.956865° large-twist BG using vdW energy densities corresponding to the KC-1 (first column) and the KC-2 models (second column). The color density plots of the total energy density in Figs. 15a and 15b highlight the honeycomb and triangular dislocation networks and match well with those from atomistic simulations (see Fig. 4). As expected, the energy density in the domain interiors is zero as they correspond to the low-energy AB and $\Sigma 7$ stackings. Figs. 15c and 15d compare the displacement jumps in the atomistic and continuum simulations.¹⁵ The displacement plots show that the core widths agree well for the KC-1 model, while the atomistic core width is relatively more diffused for the KC-2 model.

¹⁵Recall from footnote 5, that the calculation of the Burgers vectors from the diffused displacement jump of atomistic simulations is approximate. The Burgers vector can be computed exactly from the simulations of the GFK model by considering a Burgers circuit formed by directed lines $\mathbf{l}_t = \mathbf{l}$ and $\mathbf{l}_b = -\mathbf{l}$ in the deformed configurations of the top and bottom lattices, respectively. The directed line \mathbf{l} crosses a dislocation line and connects centers of two adjacent $\Sigma 7/\Sigma 1$ stackings and back. By construction, the Burgers circuit is arbitrarily thin, and its normal lies in the interface. Under this setting, the Burgers vector can be measured as

$$\int_{\mathbf{l}} (\mathbf{H}_t^{-1} - \mathbf{H}_b^{-1}) d\mathbf{l}.$$

We have confirmed using the above equation that all simulations presented in this section recover the bicrystallography-predicted Burgers vector.



(a) displacement magnitude - atomistics (b) displacement magnitude - FK model (c) energy density - FK model
 Figure 16: Simulation results of a heterostrained 21.786789° large-twist BG.

Fig. 16 shows continuum simulation results of a heterostrained 21.786789° ($\Sigma 7$) twisted BG using the vdW energy density of the KC-2 model. The displacement magnitude plotted in Fig. 16b compares well with the plot of atomistic displacement magnitude in Fig. 16a. We note that the maximum displacement in the continuum simulation is smaller compared to that in the atomistic simulation. The dislocation network is not as conspicuous in the energy density plot in Fig. 16c as it was in the earlier simulations. We attribute this feature to the diffused dislocation network noted in Fig. 15d. We note that magnitude of the energy density shown in Fig. 16c does not match with that in Figs. 6a and 6b due to the atomic energy density variation of the $\Sigma 7$ configuration, as noted in Section 2.2.

6. Summary and conclusions

Tuning quantum mechanical properties with atomic-scale precision is at the core of scientific efforts geared towards ushering in the second quantum revolution [Dowling and Milburn, 2003]. New vdW materials and heterostructures are one of the key types of the novel materials that are being explored in this regard, and provide tremendous opportunities for the field of straintronics. The design and development of vdW heterostructures with tailored properties hinge on the ability to efficiently parse heterostrains and predict the properties of the resulting moiré superlattices. Within this context, this paper focuses on predicting atomic reconstruction in vdW heterostructures efficiently by developing a generalized Frenkel-Kontorova (GFK) model.

Motivated by dislocations-mediated structural relaxation in a twisted BG, the development of the model was spurred by the following questions — a) under what heterodeformations does a vdW heterostructure undergo structural relaxation?; b) is the relaxation dislocations-mediated?; and c) how are dislocations defined in heterostructures? In our study, large twist BG serves as a surrogate for heterostructures. Noting the cusp-like local minima at an angle of 21.786789° in the plot of interface energy versus the twist angle of a BG is a signature of defect nucleation, we hypothesized that a heterostrained 21.786789° large-twist BG will undergo dislocations-mediated atomic reconstruction. Using atomistic simulations of 21.786789° large-twist BG subjected to small heterotwists and heterostrains, we confirmed our hypothesis and probed the above questions. The following key observations were made in our atomistic simulations:

1. Structural relaxation occurs via strain localization along a network of lines, which suggests it is dislocations-mediated. More interestingly, unlike the small twist case, the measured displacement jump/Burgers vectors were smaller than the smallest lattice vector of graphene.
2. Similar to the small-twist case, structural relaxation is characterized by regions of low-energy stacking interspersed by line defects. The defect-free 21.786789° stacking is the analog of the low energy AB-stacking observed in a small-twist BG.

To reveal the crystallographic origins of the observed dislocations, we explored the definition of an interface dislocation. Using SNF bicrystallography, which employs the Smith normal form for integer matrices, we showed that a heterointerface is translationally invariant with respect to translations in the DSCL. In other words, the GSFE of the defect-free 21.786789° twisted BG is periodic with respect to the DSCL, which implies the Burgers vector of interface dislocations belongs to the DSCL. The GSFE from atomistics, and its periodicity inferred from SNF bicrystallography, are used to construct the interfacial energy of the GFK model.

Inspired by crystal plasticity models, the GFK model includes three configurations — reference, natural, and deformed. The defect-free 21.786789° BG serves as the stress-free natural configuration, and the reference configuration is the natural configuration subjected to a uniform heterodeformation. By prescribing the constitutive law (interfacial energy and elastic energy) with respect to the natural configuration, the GFK model is rendered frame-invariant. The GFK model was used to simulate various heterodeformed BGs, and it was validated by comparing its predictions to those from atomistics.

We conclude by emphasizing the immense potential of the GFK model to probe the enormous heterostructure-heterostrain space for correlated electron physics. Although the model is classical and focuses on structural prediction, it can serve as — a) a workhorse for predicting structural relaxation in inhomogeneously strained heterointerfaces and b) provide a predictor for structural relaxation under uniform deformation, which can be further corrected using machine learning-based first-principles calculations [Pathrudkar et al., 2023].

7. Acknowledgements

NCA and TA would like to acknowledge support from the National Science Foundation Grant NSF-MOMS-2239734 with S. Qidwai as the program manager. ASB and CW would like to acknowledge support through grant DE-SC0023432 funded by the U.S. Department of Energy, Office of Science. ASB and CW also acknowledge computational resource support from UCLA’s Institute for Digital Research and Education (IDRE), and the National Energy Research Scientific Computing Center (NERSC awards BES-ERCAP0025205 and BES-ERCAP0025168), a DOE Office of Science User Facility supported by the Office of Science of the U.S. Department of Energy under Contract No. DE-AC02-05CH11231.

CRedit author statement

Md Tusher Ahmed: Software, Validation, Formal analysis, Investigation, Data Curation, Writing-Original Draft, Visualization, **Chenhaoyue Wang:** Software, Investigation. **Amartya S. Banerjee:** Software, Investigation, Resources, Writing-Review & Editing, Supervision, Funding acquisition **Nikhil Chandra Admal:** Conceptualization, Methodology, Software, Formal analysis, Investigation, Resources, Writing-Review & Editing, Supervision, Project Management, Funding acquisition.

Appendix A. Coincidence relation between two lattices

In this section, we will develop an algorithm to enumerate heterodeformations that result in moiré superlattices. Let \mathcal{A} and \mathcal{B} denote two 2D lattices with structure matrices \mathbf{A} and \mathbf{B} , respectively. It is easy to see that the lattices coincide on a moiré superlattice if and only if the transition matrix, $\mathbf{T} := \mathbf{A}^{-1}\mathbf{B}$, is rational. However, this condition is invariably not satisfied and a heterodeformation is required to form a moiré supercell. Therefore, we are interested in all distortions \mathbf{F} of lattice \mathcal{A} , such that the deformed lattice shares a moiré supercell with \mathcal{B} . In other words, we would like to compute all \mathbf{F} such that the transition matrix

$$\mathbf{T} = \mathbf{B}^{-1}\mathbf{F}\mathbf{A} \text{ is rational.} \tag{A.1}$$

Moreover, since large elastic strain are energetically unfavorable, we are only interested in heterodeformations that lead to small stretches. Heterotwists are included in this search as they cost no elastic energy.

A general solution to (A.1) is given by the following theorem (see Admal et al. [2022]):

Theorem 2. Let \mathcal{A} and \mathcal{B} be two 2D lattices forming a heterostructure, and \mathbf{F} an in-plane linear transformation. Then, $\mathcal{A} \cap \mathbf{F}\mathcal{B}$ is a 2D moiré superlattice if and only if there exist lattice vectors \mathbf{q}_1 and \mathbf{r}_1 in \mathcal{B} , and \mathbf{q}_2 and \mathbf{r}_2 in \mathcal{A} such that

$$\mathbf{q}_2 = \alpha \mathbf{F} \mathbf{q}_1, \quad \mathbf{r}_2 = \beta \mathbf{F} \mathbf{r}_1 \quad (\text{A.2})$$

for some rationals α and β . Moreover, \mathbf{F} is given by

$$\mathbf{F} = \frac{1}{\alpha} \mathbf{q}_2 \otimes \boldsymbol{\varphi}_1 + \frac{1}{\beta} \mathbf{r}_2 \otimes \boldsymbol{\varphi}_1, \quad (\text{A.3})$$

where $\boldsymbol{\varphi}_1, \boldsymbol{\varphi}_1 \in \mathcal{B}^*$ (dual/reciprocal lattice of \mathcal{B}) such that $\boldsymbol{\varphi}_1 \cdot \mathbf{q}_1 = \boldsymbol{\varphi}_1 \cdot \mathbf{r}_1 = 1$.

An algorithm to construct \mathbf{F} given in (A.3) can be found in Admal et al. [2022], and it is implemented in oILAB.

Appendix B. Smith normal form bicrystallography

In this section, we introduce SNF bicrystallography, a framework to analyze the crystallography of heterostructures. In this paper, SNF bicrystallography is used to calculate the DSCL of a heterostructure, and plays a central role in our definition of interface dislocation, introduced in Section 3. We refer the reader to Admal et al. [2022] for a more detailed presentation.

Let \mathcal{A} and \mathcal{B} denote 2D lattices that form a moiré superlattice. From Appendix A, we know that the transition matrix $\mathbf{T} = \mathbf{A}^{-1} \mathbf{B}$ is rational. Therefore, \mathbf{T} can be expressed as

$$\mathbf{T} = \frac{\mathbf{P}}{\mu}, \quad (\text{B.1})$$

where μ is an integer, and \mathbf{P} is an integer matrix such that μ and the entries of \mathbf{P} are co-prime. Using the Smith normal form for integer matrices, \mathbf{P} can be multiplicatively decomposed as

$$\mathbf{P} = \mathbf{U} \boldsymbol{\Delta} \mathbf{V}^{-1}, \quad (\text{B.2})$$

where \mathbf{U} and \mathbf{V} are unimodular matrices, and $\boldsymbol{\Delta} = \text{diag}(\delta_1, \delta_2)$ is a diagonal matrix and $\delta_1 = \text{gcd}(\mathbf{P})$. Substituting (B.2) into (B.1) and rearranging, we have

$$\mu \mathbf{B}^{\parallel} = \mathbf{A}^{\parallel} \boldsymbol{\Delta}, \quad \text{where} \quad (\text{B.3})$$

$$\mathbf{A}^{\parallel} = \mathbf{A} \mathbf{U}, \quad \text{and} \quad \mathbf{B}^{\parallel} = \mathbf{B} \mathbf{V}. \quad (\text{B.4})$$

Since \mathbf{U} and \mathbf{V} are unimodular, the matrices \mathbf{A}^{\parallel} and \mathbf{B}^{\parallel} qualify as new structure matrices of lattices \mathcal{A} and \mathcal{B} , respectively. In other words, the columns $\{\mathbf{a}_i^{\parallel}\}$ and $\{\mathbf{b}_i^{\parallel}\}$ of \mathbf{A}^{\parallel} and \mathbf{B}^{\parallel} are the new bases of the two lattices. Since $\boldsymbol{\Delta}$ is a diagonal matrix, Eq. (B.3) reads as,

$$\mu \mathbf{b}_i^{\parallel} = \delta_i \mathbf{a}_i^{\parallel} \quad (\text{no summation over } i). \quad (\text{B.5})$$

(B.5) implies the new bases are parallel and coincide on the CSL \mathcal{C} with basis vectors

$$\mathbf{c}_i^{\parallel} = \frac{\mu}{\text{gcd}(\mu, \delta_i)} \mathbf{b}_i^{\parallel} = \frac{\delta_i}{\text{gcd}(\mu, \delta_i)} \mathbf{a}_i^{\parallel}. \quad (\text{B.6})$$

The basis vectors $\{\mathbf{c}_1^{\parallel}, \mathbf{c}_2^{\parallel}\}$ of \mathcal{C} can be collected in a structure matrix as

$$\mathbf{C}^{\parallel} = \mathbf{B}^{\parallel} \mathbf{N} = \mathbf{A}^{\parallel} \mathbf{M}. \quad (\text{B.7})$$

where

$$\mathbf{M} = \text{diag} \left(\frac{\delta_i}{\text{gcd}(\mu, \delta_i)} \right) \quad \text{and} \quad \mathbf{N} = \text{diag} \left(\frac{\mu}{\text{gcd}(\mu, \delta_i)} \right), \quad (\text{B.8})$$

are auxiliary diagonal matrices satisfying the relation $\mu\mathbf{M} = \mathbf{\Delta}\mathbf{N}$.

The DSCL, denoted as \mathcal{D} , is the smallest lattice that contains lattices \mathcal{A} and \mathcal{B} . The basis vectors $\{\mathbf{d}_1^{\parallel}, \mathbf{d}_2^{\parallel}\}$ of \mathcal{D} are given by

$$\mathbf{d}_i^{\parallel} = \frac{\text{gcd}(\mu, \delta_i)}{\delta_i} \mathbf{b}_i^{\parallel} = \frac{\text{gcd}(\mu, \delta_i)}{\mu} \mathbf{a}_i^{\parallel}. \quad (\text{B.9})$$

(B.8) and (B.9) imply the structure matrix of \mathcal{D} satisfies

$$\mathbf{D}^{\parallel} = \mathbf{B}^{\parallel} \mathbf{M}^{-1} = \mathbf{A}^{\parallel} \mathbf{N}^{-1}. \quad (\text{B.10})$$

(B.7) and (B.10) imply the ratios of areas of primitive unit cells

$$\Sigma_{\mathcal{A}} := \frac{\det \mathbf{C}^{\parallel}}{\det \mathbf{A}^{\parallel}} = \det \mathbf{M}, \quad \Sigma_{\mathcal{B}} := \frac{\det \mathbf{C}^{\parallel}}{\det \mathbf{B}^{\parallel}} = \det \mathbf{N} \quad (\text{B.11})$$

are integers, and $\det(\mathbf{C}) \det(\mathbf{D}) = \det(\mathbf{A}) \det(\mathbf{B})$.

The parallel bases for \mathcal{A} , \mathcal{B} , \mathcal{C} , and \mathcal{D} highlight an interesting analogy with the notions of least common multiple (lcm) and greatest common divisor (gcd) of integers. The CSL and the DSCL may be interpreted as the lcm and the gcd of lattices \mathcal{A} and \mathcal{B} , respectively.

We will now demonstrate the application of SNF bicrystallography to the 21.786789° twisted BG. Let \mathcal{A} represent the hexagonal lattice of graphene with structure matrix

$$\mathbf{A} = \frac{a}{2} \begin{bmatrix} 0 & -\sqrt{3} \\ 2 & -1 \end{bmatrix},$$

where the lattice constant of graphene is assumed to be $a = 2.46\text{\AA}$. Let \mathcal{B} represent another hexagonal lattice twisted anti-clockwise relative to \mathcal{A} , i.e.

$$\mathbf{B} = \mathbf{R}_\theta \mathbf{A}.$$

where $\theta = 21.786789^\circ$ guarantees a coincidence between the lattices with a rational transition matrix

$$\mathbf{T} = \mathbf{A}^{-1} \mathbf{B} = \frac{1}{7} \begin{bmatrix} 5 & -8 \\ 8 & -3 \end{bmatrix}, \quad (\text{B.12})$$

The SNF of the integer matrix in (B.12) yields

$$\mathbf{\Delta} = \text{diag}(1, 49), \quad \mathbf{U} = \begin{bmatrix} 19 & 1 \\ 1 & 0 \end{bmatrix}, \quad \mathbf{V} = \begin{bmatrix} -1 & -3 \\ -3 & -8 \end{bmatrix}, \quad \mathbf{M} = \text{diag}(1, 7), \quad \mathbf{N} = \text{diag}(7, 1).$$

The basis vectors of the CSL and the DSCL can be obtained using (B.7) and (B.10). The basis vectors of \mathcal{C} are used to define the periodic box of our atomistic and continuum simulations, while those of \mathcal{D} are used to identify the Burgers vectors of interface dislocations. While the parallel bases are valuable in proving statements such as Theorem 1, the corresponding structure matrices are typically ill-conditioned. Therefore, we resort to lattice reduction algorithms to obtain reduced bases from the parallel bases.

Appendix C. Computational details of density functional theory calculations of the GSFE of 21.786789° twisted bilayer graphene

First-principles calculations using Density Functional Theory (DFT) were performed to calculate the GSFE of 21.786789° twisted bilayer graphene (TBG), via the Quantum Espresso package [Giannozzi et al., 2009]. Projector augmented wave (PAW) type pseudopotentials [Blöchl et al., 2002], along with the generalized gradient approximation (Perdew-Burke-Ernzerhof functional [Perdew et al., 1998]) and Grimme's density functional dispersion correction (DFT-D2) [Grimme et al., 2011] were employed to calculate the GSFE landscape of BG systems. These choices allowed us to balance computational accuracy and efficiency, and are also consistent with earlier literature [Zhou et al., 2015]. The interlayer spacing was set to 2.46\AA ,

inducing 26% out-of-plane compression in the BG system. In-plane periodic boundary conditions, and out-of-plane isolated system conditions were adopted to simulate the two-dimensional nature of the system. The values of the planewave cutoff energy ($E_{\text{cut}} = 70$ Rydbergs) and k-point mesh parameters were optimized to ensure the total energy of systems converged to 0.001 eV in all calculations. The GSFE calculation was conducted by taking displacement on a $15 \times 15 \times 1$ mesh of two lattice vectors, $\mathbf{b}_1 = -0.929792342 \mathbf{e}_1$, and $\mathbf{b}_2 = -0.464896163 \mathbf{e}_1 + 0.805223601 \mathbf{e}_2$.

Appendix D. Comparison with the small-twist BG model of Nam and Koshino [2017]

In this section, we will specialize the GFK model to small-twist homostructures by invoking isotropic linear elasticity to recover the model of Nam and Koshino [2017], which was developed to model atomic reconstruction in small-twist BG.

The Frenkel–Kontorova model of Nam and Koshino [2017] for small-twist BG was formulated in terms of a single unknown field \mathbf{u}_- , which denotes the difference in the displacement fields of the top and bottom lattices. We will now show that under small deformations, the Nam and Koshino [2017] model can be recovered from the GFK model of Section 4.

Introducing the displacement variables $\mathbf{u}_\alpha := \phi_\alpha(\mathbf{X}, t) - \mathbf{X}$, and $\mathbf{u}_\pm = \mathbf{u}_t \pm \mathbf{u}_b$, we first express \mathcal{E} as a functional of \mathbf{u}_+ and \mathbf{u}_- under the assumption of small deformation. Notice that we are using the variable \mathbf{X} , as opposed to \mathbf{X}_α , since the two reference configurations coincide under PBCs. Beginning with \mathcal{E}_{el} , we invoke linear elasticity by writing the elastic energy density as

$$e_{\text{el}}(\boldsymbol{\epsilon}_\alpha) = \frac{1}{2} \mathbb{C} \boldsymbol{\epsilon}_\alpha \cdot \boldsymbol{\epsilon}_\alpha = \lambda (\text{tr } \boldsymbol{\epsilon}_\alpha)^2 + 2\mu \boldsymbol{\epsilon}_\alpha \cdot \boldsymbol{\epsilon}_\alpha, \quad (\text{D.1})$$

where the Lagrangian strain in (13) has been replaced by the infinitesimal strain $\boldsymbol{\epsilon}_\alpha = (\nabla \mathbf{u}_\alpha + \nabla \mathbf{u}_\alpha^T)/2$, and \mathbb{C} is the fourth-order isotropic elasticity tensor with lamé constants λ and μ . Under this setting, \mathcal{E}_{el} can be recast as a functional of \mathbf{u}_+ and \mathbf{u}_- as follows:

$$\mathcal{E}_{\text{el}}[\mathbf{u}_+, \mathbf{u}_-] = \frac{1}{4} \int_{\Omega_{\text{ref}}} (\mathbb{C} \boldsymbol{\epsilon}_+ \cdot \boldsymbol{\epsilon}_+ + \mathbb{C} \boldsymbol{\epsilon}_- \cdot \boldsymbol{\epsilon}_-) d\mathbf{X}. \quad (\text{D.2})$$

where $\boldsymbol{\epsilon}_\pm := (\nabla \mathbf{u}_\pm + \nabla \mathbf{u}_\pm^T)/2$. Next, assuming a) $\det \mathbf{K}_\alpha \approx \det \mathbf{F}_\alpha \approx 1$ and b) $\mathbf{H}_\alpha \approx \mathbf{I}$, the vdW energy can be expressed as a functional exclusively of \mathbf{u}_- :

$$\mathcal{E}_{\text{vdW}}[\mathbf{u}_-] = \int_{\Omega_{\text{ref}}} e_{\text{vdW}}(\mathbf{r}(\mathbf{X})) d\mathbf{X}, \quad (\text{D.3})$$

where $\mathbf{r}(\mathbf{X})$, given by (11), is written as $\mathbf{r}(\mathbf{X}) = (\mathbf{K}_t - \mathbf{K}_b)\mathbf{X} - \mathbf{u}_-(\mathbf{X})$ since $\phi_t - \phi_b = \mathbf{u}_t - \mathbf{u}_b = \mathbf{u}_-$.

Since \mathcal{E}_{vdW} in (D.3) is independent of \mathbf{u}_+ , it is easy to see that minimizing the total energy functional $\mathcal{E}[\mathbf{u}_+, \mathbf{u}_-]$ results in $\mathbf{u}_+ \equiv 0$, which allowed Nam and Koshino [2017] to cast their total energy functional in the single variable \mathbf{u}_- :

$$\mathcal{E}[\mathbf{u}_-] = \int_{\Omega_{\text{ref}}} \left(\frac{1}{4} \mathbb{C} \boldsymbol{\epsilon}_- \cdot \boldsymbol{\epsilon}_- + e_{\text{vdW}}(\mathbf{r}) \right) d\mathbf{X}. \quad (\text{D.4})$$

References

- Nikhil Chandra Admal, Giacomo Po, and Jaime Marian. A unified framework for polycrystal plasticity with grain boundary evolution. *International Journal of Plasticity*, 106:1–30, 2018. ISSN 0749-6419. doi: <https://doi.org/10.1016/j.ijplas.2018.01.014>. URL <https://www.sciencedirect.com/science/article/pii/S0749641917305557>.
- Nikhil Chandra Admal, Tusher Ahmed, Enrique Martinez, and Giacomo Po. Interface dislocations and grain boundary disconnections using smith normal bicrystallography. *Acta Materialia*, 240:118340, 2022. ISSN 1359-6454. doi: <https://doi.org/10.1016/j.actamat.2022.118340>. URL <https://www.sciencedirect.com/science/article/pii/S1359645422007194>.

- Jonathan S Alden, Adam W Tsen, Pinshane Y Huang, Robert Hovden, Lola Brown, Jiwoong Park, David A Muller, and Paul L McEuen. Strain solitons and topological defects in bilayer graphene. *Proceedings of the National Academy of Sciences*, 110(28):11256–11260, 2013.
- Emil Annevelink, Harley T. Johnson, and Elif Ertekin. Topologically derived dislocation theory for twist and stretch moiré superlattices in bilayer graphene. *Phys. Rev. B*, 102:184107, Nov 2020. doi: 10.1103/PhysRevB.102.184107. URL <https://link.aps.org/doi/10.1103/PhysRevB.102.184107>.
- Emil Annevelink, Zhu-Jun Wang, Guocai Dong, Harley T Johnson, and Pascal Pochet. A moiré theory for probing grain boundary structure in graphene. *Acta Materialia*, 217:117156, 2021.
- R W Balluffi, A Brokman, and A H King. Csl/dsc lattice model for general crystal boundaries and their line defects. *Acta Metall.; (United States)*, 30:8, 8 1982. doi: 10.1016/0001-6160(82)90166-3. URL <https://www.osti.gov/biblio/5907589>.
- DN Basov, RD Averitt, and D Hsieh. Towards properties on demand in quantum materials. *Nature materials*, 16(11):1077–1088, 2017.
- Rafi Bistritzer and Allan H. MacDonald. Moiré bands in twisted double-layer graphene. *Proceedings of the National Academy of Sciences*, 108(30):12233–12237, 2011. doi: 10.1073/pnas.1108174108. URL <https://www.pnas.org/doi/abs/10.1073/pnas.1108174108>.
- Erik Bitzek, Pekka Koskinen, Franz Gähler, Michael Moseler, and Peter Gumbsch. Structural relaxation made simple. *Phys. Rev. Lett.*, 97:170201, Oct 2006. doi: 10.1103/PhysRevLett.97.170201. URL <https://link.aps.org/doi/10.1103/PhysRevLett.97.170201>.
- Peter E. Blöchl, Clemens J. Först, and Johannes Schimpl. The Projector Augmented Wave Method: Ab-initio molecular dynamics with full wave functions, July 2002.
- Donald W Brenner, Olga A Shenderova, Judith A Harrison, Steven J Stuart, Boris Ni, and Susan B Sinnott. A second-generation reactive empirical bond order (rebo) potential energy expression for hydrocarbons. *Journal of Physics: Condensed Matter*, 14(4):783, jan 2002. doi: 10.1088/0953-8984/14/4/312. URL <https://dx.doi.org/10.1088/0953-8984/14/4/312>.
- Yuan Cao, Valla Fatemi, Shiang Fang, Kenji Watanabe, Takashi Taniguchi, Efthimios Kaxiras, and Pablo Jarillo-Herrero. Unconventional superconductivity in magic-angle graphene superlattices. *Nature*, 556(7699):43–50, April 2018. ISSN 1476-4687. doi: 10.1038/nature26160. URL <https://www.nature.com/articles/nature26160>.
- Yuan Cao, Daniel Rodan-Legrain, Oriol Rubies-Bigorda, Jeong Min Park, Kenji Watanabe, Takashi Taniguchi, and Pablo Jarillo-Herrero. Tunable correlated states and spin-polarized phases in twisted bilayer–bilayer graphene. *Nature*, 583(7815):215–220, 2020. doi: 10.1038/s41586-020-2260-6.
- Yuan Cao, Daniel Rodan-Legrain, Jeong Min Park, Noah F. Q. Yuan, Kenji Watanabe, Takashi Taniguchi, Rafael M. Fernandes, Liang Fu, and Pablo Jarillo-Herrero. Nematicity and competing orders in superconducting magic-angle graphene. *Science*, 372(6539):264–271, 2021. doi: 10.1126/science.abc2836. URL <https://www.science.org/doi/abs/10.1126/science.abc2836>.
- Stephen Carr, Shiang Fang, Pablo Jarillo-Herrero, and Efthimios Kaxiras. Pressure dependence of the magic twist angle in graphene superlattices. *Phys. Rev. B*, 98:085144, Aug 2018a. doi: 10.1103/PhysRevB.98.085144. URL <https://link.aps.org/doi/10.1103/PhysRevB.98.085144>.
- Stephen Carr, Daniel Massatt, Steven B. Torrisi, Paul Cazeaux, Mitchell Luskin, and Efthimios Kaxiras. Relaxation and domain formation in incommensurate two-dimensional heterostructures. *Phys. Rev. B*, 98:224102, Dec 2018b. doi: 10.1103/PhysRevB.98.224102. URL <https://link.aps.org/doi/10.1103/PhysRevB.98.224102>.
- Paul Cazeaux, Mitchell Luskin, and Daniel Massatt. Energy minimization of two dimensional incommensurate heterostructures. *Archive for Rational Mechanics and Analysis*, 235(2):1289–1325, 2020.

- Paul Cazeaux, Drake Clark, Rebecca Engelke, Philip Kim, and Mitchell Luskin. Relaxation and domain wall structure of bilayer moire systems. *Journal of Elasticity*, pages 1–24, 2023.
- Xiaobian Cheng, Jie Yuan, Benhu Zhou, and Benliang Zhou. The moiré pattern rule of the twisted bilayer graphene and its electronic property under a strain. *The European Physical Journal Plus*, 138(1):1–6, 2023.
- Bheema Lingam Chittari, Nicolas Leconte, Srivani Javvaji, and Jeil Jung. Pressure induced compression of flatbands in twisted bilayer graphene. *Electronic Structure*, 1(1):015001, nov 2018. doi: 10.1088/2516-1075/aaead3. URL <https://dx.doi.org/10.1088/2516-1075/aaead3>.
- John D Clayton. *Nonlinear mechanics of crystals*, volume 177. Springer Science & Business Media, 2010.
- Shuyang Dai, Yang Xiang, and David J. Srolovitz. Twisted bilayer graphene: Moiré with a twist. *Nano Letters*, 16(9):5923–5927, 2016. doi: 10.1021/acs.nanolett.6b02870.
- Deya Das, Swastibrata Bhattacharyya, Enrique Muñoz, and Abhishek K. Singh. Strain-induced chiral symmetry breaking leads to large dirac cone splitting in graphene/graphane heterostructure. *Phys. Rev. B*, 94:115438, Sep 2016. doi: 10.1103/PhysRevB.94.115438. URL <https://link.aps.org/doi/10.1103/PhysRevB.94.115438>.
- Jonathan P Dowling and Gerard J Milburn. Quantum technology: the second quantum revolution. *Philosophical Transactions of the Royal Society of London. Series A: Mathematical, Physical and Engineering Sciences*, 361(1809):1655–1674, 2003.
- Fernando Gargiulo and Oleg V Yazyev. Structural and electronic transformation in low-angle twisted bilayer graphene. *2D Materials*, 5(1):015019, nov 2017. doi: 10.1088/2053-1583/aa9640. URL <https://dx.doi.org/10.1088/2053-1583/aa9640>.
- Paolo Giannozzi, Stefano Baroni, Nicola Bonini, Matteo Calandra, Roberto Car, Carlo Cavazzoni, Davide Ceresoli, Guido L. Chiarotti, Matteo Cococcioni, Ismaila Dabo, Andrea Dal Corso, Stefano de Gironcoli, Stefano Fabris, Guido Fratesi, Ralph Gebauer, Uwe Gerstmann, Christos Gougoussis, Anton Kokalj, Michele Lazzeri, Layla Martin-Samos, Nicola Marzari, Francesco Mauri, Riccardo Mazzarello, Stefano Paolini, Alfredo Pasquarello, Lorenzo Paulatto, Carlo Sbraccia, Sandro Scandolo, Gabriele Sclauzero, Ari P. Seitsonen, Alexander Smogunov, Paolo Umari, and Renata M. Wentzcovitch. QUANTUM ESPRESSO: A modular and open-source software project for quantum simulations of materials. *J. Phys.: Condens. Matter*, 21(39):395502, September 2009. ISSN 0953-8984. doi: 10.1088/0953-8984/21/39/395502.
- Stefan Grimme, Stephan Ehrlich, and Lars Goerigk. Effect of the damping function in dispersion corrected density functional theory. *Journal of Computational Chemistry*, 32(7):1456–1465, 2011. ISSN 1096-987X. doi: 10.1002/jcc.21759.
- H Grimmer, WT Bollmann, and DH Warrington. Coincidence-site lattices and complete pattern-shift in cubic crystals. *Acta Crystallographica Section A: Crystal Physics, Diffraction, Theoretical and General Crystallography*, 30(2):197–207, 1974.
- Matthew J. Hamer, Alessio Giampietri, Viktor Kandyba, Francesca Genuzio, Tevfik O. Mentş, Andrea Locatelli, Roman V. Gorbachev, Alexei Barinov, and Marcin Mucha-Kruczyński. Moiré superlattice effects and band structure evolution in near-30-degree twisted bilayer graphene. *ACS Nano*, 16(2):1954–1962, 2022. doi: 10.1021/acsnano.1c06439. URL <https://doi.org/10.1021/acsnano.1c06439>. PMID: 35073479.
- Junyan He and Nikhil Chandra Admal. Polycrystal plasticity with grain boundary evolution: A numerically efficient dislocation-based diffuse-interface model. *Modelling and Simulation in Materials Science and Engineering*, 30, 10 2021. doi: 10.1088/1361-651X/ac2f84.
- M Yousuff Hussaini and Thomas A Zang. Spectral methods in fluid dynamics. *Annual review of fluid mechanics*, 19(1):339–367, 1987.

- Ryo Ishikawa, Nathan R Lugg, Kazutoshi Inoue, Hidetaka Sawada, Takashi Taniguchi, Naoya Shibata, and Yuichi Ikuhara. Interfacial atomic structure of twisted few-layer graphene. *Scientific reports*, 6(1):21273, 2016.
- Chenhao Jin, Emma C. Regan, Aiming Yan, M. Iqbal Bakti Utama, Danqing Wang, Sihan Zhao, Ying Qin, Sijie Yang, Zhiren Zheng, Shenyang Shi, Kenji Watanabe, Takashi Taniguchi, Sefaattin Tongay, Alex Zettl, and Feng Wang. Observation of moiré excitons in wse₂/ws₂ heterostructure superlattices. *Nature (London)*, 567(7746), 2 2019.
- Himanshu Joshi, Junyan He, and Nikhil Chandra Admal. A finite deformation theory for grain boundary plasticity based on geometrically necessary disconnections. *Journal of the Mechanics and Physics of Solids*, 167:104949, 06 2022. doi: 10.1016/j.jmps.2022.104949.
- B Keimer and JE Moore. The physics of quantum materials. *Nature Physics*, 13(11):1045–1055, 2017.
- Jin Myung Kim, Md Farhadul Haque, Ezekiel Y Hsieh, Shahriar Muhammad Nahid, Ishrat Zarin, Kwang-Yong Jeong, Jae-Pil So, Hong-Gyu Park, and SungWoo Nam. Strain engineering of low-dimensional materials for emerging quantum phenomena and functionalities. *Advanced Materials*, page 2107362, 2022.
- Kyoungwan Kim, Matthew Yankowitz, Babak Fallahazad, Sangwoo Kang, Hema CP Movva, Shengqiang Huang, Stefano Larentis, Chris M Corbet, Takashi Taniguchi, Kenji Watanabe, et al. van der waals heterostructures with high accuracy rotational alignment. *Nano letters*, 16(3):1989–1995, 2016.
- Daniel S Koda, Friedhelm Bechstedt, Marcelo Marques, and Lara K Teles. Coincidence lattices of 2d crystals: Heterostructure predictions and applications. *The Journal of Physical Chemistry C*, 120(20):10895–10908, 2016.
- Aleksey N. Kolmogorov and Vincent H. Crespi. Registry-dependent interlayer potential for graphitic systems. *Phys. Rev. B*, 71:235415, Jun 2005. doi: 10.1103/PhysRevB.71.235415. URL <https://link.aps.org/doi/10.1103/PhysRevB.71.235415>.
- Hemant Kumar, Liang Dong, and Vivek B Shenoy. Limits of coherency and strain transfer in flexible 2d van der waals heterostructures: formation of strain solitons and interlayer debonding. *Scientific reports*, 6(1): 21516, 2016.
- Jin-Ho Lee, Soo-jeong Park, and Jeong-Woo Choi. Electrical property of graphene and its application to electrochemical biosensing. *Nanomaterials*, 9(2):297, 2019. doi: 10.3390/nano9020297.
- J. M. B. Lopes dos Santos, N. M. R. Peres, and A. H. Castro Neto. Continuum model of the twisted graphene bilayer. *Phys. Rev. B*, 86:155449, Oct 2012. doi: 10.1103/PhysRevB.86.155449. URL <https://link.aps.org/doi/10.1103/PhysRevB.86.155449>.
- Feng Miao, Shi-Jun Liang, and Bin Cheng. Straintronics with van der waals materials. *npj Quantum Materials*, 6(1):59, 2021.
- Vahid Morovati, Zhiming Xue, Kenneth M Liechti, and Rui Huang. Interlayer coupling and strain localization in small-twist-angle graphene flakes. *Extreme Mechanics Letters*, 55:101829, 2022.
- Nguyen NT Nam and Mikito Koshino. Lattice relaxation and energy band modulation in twisted bilayer graphene. *Physical Review B*, 96(7):075311, 2017.
- Wengen Ouyang, Davide Mandelli, Michael Urbakh, and Oded Hod. Nanoserpents: Graphene nanoribbon motion on two-dimensional hexagonal materials. *Nano letters*, 18(9):6009–6016, 2018.
- Dimitrios G. Papageorgiou, Ian A. Kinloch, and Robert J. Young. Mechanical properties of graphene and graphene-based nanocomposites. *Progress in Materials Science*, 90:75–127, 2017. ISSN 0079-6425. doi: <https://doi.org/10.1016/j.pmatsci.2017.07.004>. URL <https://www.sciencedirect.com/science/article/pii/S0079642517300968>.

- Shashank Pathrudkar, Ponkrshnan Thiagarajan, Shivang Agarwal, Amartya S Banerjee, and Susanta Ghosh. Electronic structure prediction of multi-million atom systems through uncertainty quantification enabled transfer learning. *arXiv preprint arXiv:2308.13096*, 2023.
- J. P. Perdew, K. Burke, and M. Ernzerhof. Perdew, Burke, and Ernzerhof Reply:. *Phys. Rev. Lett.*, 80(4): 891–891, January 1998. doi: 10.1103/PhysRevLett.80.891.
- Steve Plimpton. Fast parallel algorithms for short-range molecular dynamics. *Journal of computational physics*, 117(1):1–19, 1995.
- Pascal Pochet, Brian C. McGuigan, Johann Coraux, and Harley T. Johnson. Toward moiré engineering in 2d materials via dislocation theory. *Applied Materials Today*, 9:240–250, 2017. ISSN 2352-9407. doi: <https://doi.org/10.1016/j.apmt.2017.07.007>. URL <https://www.sciencedirect.com/science/article/pii/S2352940717302305>.
- Tawfiqur Rakib, Pascal Pochet, Elif Ertekin, and Harley T. Johnson. Corrugation-driven symmetry breaking in magic-angle twisted bilayer graphene. *Communications Physics*, 5(1), 10 2022. doi: 10.1038/s42005-022-01013-y.
- Emma C. Regan, Danqing Wang, Chenhao Jin, M. Iqbal Bakti Utama, Beini Gao, Sihan Zhao, Wenyu Zhao, Zuo Cheng Zhang, Kentaro Yumigeta, Mark Blei, Johan D. Carlström, Kenji Watanabe, Takashi Taniguchi, Sefaattin Tongay, Michael Crommie, Alex Zettl, Feng Wang, and Xin Wei. Mott and generalized wigner crystal states in wse₂/ws₂ moiré superlattices. *Nature (London)*, 579(7799), 3 2020. doi: 10.1038/s41586-020-2092-4.
- Yuya Shimazaki, Ido Schwartz, Kenji Watanabe, Takashi Taniguchi, Martin Kroner, and Ataç Imamoğlu. Strongly correlated electrons and hybrid excitons in a moiré heterostructure. *Nature*, 580(7804):472–477, April 2020. ISSN 0028-0836. doi: 10.1038/s41586-020-2191-2. URL <https://doi.org/10.1038/s41586-020-2191-2>.
- Shengdan Tao, Xuanlin Zhang, Jiaojiao Zhu, Pimo He, Shengyuan Yang, Yunhao Lu, and Su-Huai Wei. Designing ultra-flat bands in twisted bilayer materials at large twist angles: Theory and application to two-dimensional indium selenide. *Journal of the American Chemical Society*, 144, 02 2022. doi: 10.1021/jacs.1c11953.
- Grigory Tarnopolsky, Alex Jura Kruchkov, and Ashvin Vishwanath. Origin of magic angles in twisted bilayer graphene. *Phys. Rev. Lett.*, 122:106405, Mar 2019. doi: 10.1103/PhysRevLett.122.106405. URL <https://link.aps.org/doi/10.1103/PhysRevLett.122.106405>.
- Yoshinori Tokura, Masashi Kawasaki, and Naoto Nagaosa. Emergent functions of quantum materials. *Nature Physics*, 13(11):1056–1068, 2017.
- Aviram Uri, Sameer Grover, Yuan Cao, John A Crosse, Kousik Bagani, Daniel Rodan-Legrain, Yuri Myasoedov, Kenji Watanabe, Takashi Taniguchi, Pilkyung Moon, et al. Mapping the twist-angle disorder and landau levels in magic-angle graphene. *Nature*, 581(7806):47–52, 2020.
- Dillon Wong, Kevin P. Nuckolls, Myungchul Oh, Biao Lian, Yonglong Xie, Sangjun Jeon, Kenji Watanabe, Takashi Taniguchi, B. Andrei Bernevig, Ali Yazdani, and et al. Cascade of electronic transitions in magic-angle twisted bilayer graphene. *Nature*, 582(7811):198–202, 2020. doi: 10.1038/s41586-020-2339-0.
- Kuan Zhang and Ellad B. Tadmor. Energy and moiré patterns in 2d bilayers in translation and rotation: A study using an efficient discrete-continuum interlayer potential. *Extreme Mechanics Letters*, 14:16–22, 2017. ISSN 2352-4316. doi: <https://doi.org/10.1016/j.eml.2016.10.010>. URL <https://www.sciencedirect.com/science/article/pii/S2352431616301821>. Mechanics and Mechanical Behavior of 2D Materials – Graphene and Beyond.
- Kuan Zhang and Ellad B. Tadmor. Structural and electron diffraction scaling of twisted graphene bilayers. *Journal of the Mechanics and Physics of Solids*, 112:225–238, 2018. ISSN 0022-5096. doi: <https://doi.org/10.1016/j.jmps.2017.12.005>. URL <https://www.sciencedirect.com/science/article/pii/S0022509617310153>.

- Xing-Ju Zhao, Yang Yang, Dong-Bo Zhang, and Su-Huai Wei. Formation of bloch flat bands in polar twisted bilayers without magic angles. *Phys. Rev. Lett.*, 124:086401, Feb 2020. doi: 10.1103/PhysRevLett.124.086401. URL <https://link.aps.org/doi/10.1103/PhysRevLett.124.086401>.
- Xing-Ju Zhao, Yang Yang, Dong-Bo Zhang, and Su-Huai Wei. Flat bands in twisted bilayers of polar two-dimensional semiconductors. *Phys. Rev. Mater.*, 5:014007, Jan 2021. doi: 10.1103/PhysRevMaterials.5.014007. URL <https://link.aps.org/doi/10.1103/PhysRevMaterials.5.014007>.
- Songsong Zhou, Jian Han, Shuyang Dai, Jianwei Sun, and David J. Srolovitz. Van der Waals bilayer energetics: Generalized stacking-fault energy of graphene, boron nitride, and graphene/boron nitride bilayers. *Phys. Rev. B*, 92(15):155438, October 2015. ISSN 1098-0121, 1550-235X. doi: 10.1103/PhysRevB.92.155438.